Research Paper

Early bombardment of the moon: Connecting the lunar crater record to the terrestrial planet formation

David Nesvorný [a,*], Fernando V. Roig [b], David Vokrouhlický [c], William F. Bottke [a], Simone Marchi [a], Alessandro Morbidelli [d], Rogerio Deienno [a]

[a] *Department of Space Studies, Southwest Research Institute, 1050 Walnut St., Suite 300, Boulder, CO 80302, United States*
[b] *Observatório Nacional, Rua Gal. Jose Cristino 77, Rio de Janeiro, RJ 20921-400, Brazil*
[c] *Institute of Astronomy, Charles University, V Holešovičkách 2, CZ–18000, Prague 8, Czech Republic*
[d] *Laboratoire Lagrange, UMR7293, Université Côte d'Azur, CNRS, Observatoire de la Côte d'Azur, Bouldervard de l'Observatoire, 06304, Nice Cedex 4, France*

A B S T R A C T

The lunar crater record features ~ 50 basins. The radiometric dating of Apollo samples indicates that the Imbrium basin formed relatively late — from the planet formation perspective — some $\simeq 3.9$ Ga. Here we develop a dynamical model for impactors in the inner solar system to provide context for the interpretation of the lunar crater record. The contribution of cometary impactors is found to be insignificant. Asteroids produced most large impacts on the terrestrial worlds in the last $\simeq 3$ Gyr. The great majority of early impactors were rocky planetesimals left behind at ~ 0.5–1.5 au after the terrestrial planet accretion. The population of terrestrial planetesimals was reduced by disruptive collisions in the first $t \sim 20$ Myr after the gas disk dispersal. We estimate that there were $\sim 4 \times 10^5$ diameter $d > 10$ km bodies when the Moon formed (total planetesimal mass ~ 0.015 M_{Earth} at $t \sim 50$ Myr). The early bombardment of the Moon was intense. To accommodate ~ 50 known basins, the lunar basins that formed before $\simeq 4.35$–4.41 Ga must have been erased. The late formation of Imbrium occurs with a ~ 15–35% probability in our model. About 20 $d > 10$-km bodies were expected to hit the Earth between 2.5 and 3.5 Ga, which is comparable to the number of known spherule beds in the late Archean. We discuss implications of our model for the lunar/Martian crater chronologies, Late Veneer, and noble gases in the Earth atmosphere.

1. Introduction

In the standard model of terrestrial planet formation (Wetherill, 1990), accretional collisions between 1 to 1000 km planetesimals lead to gradual build up of lunar- to Mars-size protoplanets that gravitationally interact and further grow during a late stage of giant impacts (Chambers and Wetherill, 1998). The hafnium–tungsten (Hf–W) isotopic system analysis indicates that the Moon-forming impact on proto-Earth happened relatively late, some $\sim$ 30–150 Myr after the appearance of the first solar system solids (Kleine and Walker, 2017; Thiemens et al., 2019, 2021; Barboni et al., 2017; Maurice et al., 2020; Kruijer et al., 2021). The new-born Moon was molten, gradually cooled down, and was eventually able to support impact structures on its surface (Meyer et al., 2010; Elkins-Tanton et al., 2011; Miljković et al., 2021). This is time zero for the lunar crater record.

The early lunar bombardment was intense (Hartmann, 1966): at least 40 and up to 90 lunar basins (crater diameter $D > 300$ km) have been recognized or proposed (e.g., Wilhelms et al., 1987; Spudis, 1993; Fassett et al., 2012). Neumann et al. (2015) used gravity anomalies observed by GRAIL to report a complete list of all $D > 200$ km craters on the whole lunar surface (both the nearside and farside). In Table 1 of Neumann et al. (2015), there are 43 basins with the main ring diameter $D > 300$ km. From crater scaling laws appropriate for the lunar gravity (e.g., Johnson et al., 2016a), a diameter $d \sim 20$ km impactor is needed to excavate a $D = 300$ km crater.[1] Miljković et al. (2016), modeling the GRAIL data from Neumann et al. (2015) with the iSALE-2D hydrocode, found that the lunar surface recorded $\simeq 50$ impacts of $d > 20$ km bodies (the impact speed ~ 20 km s^{-1} is used here to convert the C parameter reported in their Table 2 to the impactor size). Here we use the results from Neumann et al. (2015) and Miljković et al. (2016) as an important constraint on our modeling efforts.

At least some of the lunar basins formed relatively late. The radiometric dating of impact melts found in the Apollo samples indicates that

---

the Imbrium basin formed $\simeq$ 3.92 Gyr ago (Ga; Zhang et al., 2019), that is $\simeq$ 650 Myr after the first solar system solids (Bouvier et al., 2007; Burkhardt et al., 2008). The Imbrium basin was excavated by a $d \gtrsim$ 100 km impactor (Miljković et al., 2013, 2016; Schultz and Crawford, 2016). Of all the known basins, only Orientale and Schrödinger have a lower accumulated density of superposed craters than Imbrium, and must therefore be (slightly) younger than Imbrium. The Orientale basin was produced by a $d = 50$ km (Miljković et al., 2016) or $d = 64$ km (Johnson et al., 2016b) impactor. A smaller, $d \simeq 20$ km body impact is responsible for the Schrödinger basin ($D = 312$ km; Miljković et al., 2016).

Having (at least) three basin-forming impacts happening at $t \gtrsim$ 650 Myr after the first solar system solids is unexpected from the planet formation perspective. In the inner solar system, where the accretion processes have relatively short timescales (< 100 Myr; Wetherill, 1990), the impact flux should have rapidly declined over time (Bottke et al., 2007). This has motivated the impact spike hypothesis where it was assumed that the Imbrium-era impacts mark an epoch of enhanced bombardment (Tera et al., 1974; Ryder, 1990, 2002; Cohen et al., 2000; Stöffler and Ryder, 2001; Kring and Cohen, 2002), and prompted search for possible causes (e.g., Levison et al., 2001; Gomes et al., 2005). This epoch is often called the Late Heavy Bombardment (LHB). We avoid using this term here because LHB has too many strings attached to it (Hartmann, 2019).

The goal of this paper is to develop an accurate dynamical model of asteroid, comet and planetesimal impactors in the inner solar system. The model for asteroid and comet impactors is taken from previous publications (Nesvorný et al., 2017a,b). We take advantage of the recent simulations of terrestrial planet formation (Section 2) that faithfully match the masses, orbits and accretion histories of planets (Nesvorný et al., 2021a). Planetesimals remaining in these simulations after the Moon-forming impact ("leftovers") are cloned and followed for additional 1 Gyr. All impacts on the terrestrial worlds are recorded in this interval. When combined with asteroids and comets, the new impact chronology model can be compared to the lunar crater record. We find that a steadily declining impact flux — in the spirit of Hartung (1974) — provides an adequate interpretation of available data.

Initial results from this study were reported in Nesvorný et al. (2022). Here we discuss the results in detail and, in addition: (1) provide a thorough description of the methodology, simulations and impact profiles obtained under different assumptions (e.g., as a function of the number and radial extension of terrestrial planetesimals), (2) explain how and why our results differ from those obtained in previous studies (e.g., Bottke et al., 2007; Brasser et al., 2020), (3) obtain the lunar and Martian impact chronologies, discuss their relationship and implications for ages of different terrains, (4) include constraints from highly siderophile elements for the Earth, Mars, and Moon, and (5) highlight comet impactors as the source of noble gasses in the Earth atmosphere (Marty et al., 2016).

2. Terrestrial planet formation

We take advantage of our N-body simulations of the standard model (Nesvorný et al., 2021a). The simulations included, for consistency, the effects of radial migration and dynamical instability of the outer planets (Tsiganis et al., 2005). The instability was assumed to have happened early, within ~ 10 Myr after the protoplanetary disk dispersal (Clement et al., 2018). In the specific case considered here, the outer planets started in a chain of mean motion resonances (3:2 and 2:1) and the instability happened at $t = 5.8$ Myr after the gas disk dispersal. We found that the details of outer planet instability do not matter with small Mars[2] (potentially) forming even in the case where the outer planets are placed on their present orbits at the beginning of simulations.

The model with a radially extended disk of terrestrial protoplanets, however, failed to match the tight orbital spacing of Venus and Earth. To obtain the correct spacing, the terrestrial protoplanets must have started in a narrow annulus (0.7–1 au; Hansen, 2009) and have (about) the Mars mass to begin with (Jacobson and Morbidelli, 2014).[3] The tight radial spacing of Venus and Earth would be particularly easy to understand if terrestrial protoplanets convergently migrated toward ~ 0.7–1 au during the gas disk stage (Brož et al., 2021).

In the W11e/20M model from Nesvorný et al. (2021a), which we will utilize here, 20 Mars-mass protoplanets were initially ($t = 0$; marking the gas nebula dispersal) distributed in a narrow, dynamically cold annulus (orbital radius $0.7 < r < 1$ au). In addition, 1000 planetesimals with the total mass of $2\,M_{\text{Earth}}$ were placed in an extended disk ($0.3 < r < 4$ au). The radial surface density profile of planetesimals was set to $\Sigma(r) \propto r^{-1}$. We performed 100 simulations of the W11e/20M model where different seeds were used to generate slightly different initial conditions. This produced 100 growth histories of the terrestrial planets. The results were statistically analyzed using different criteria, including the number and mass of planets, their radial mass concentration, the angular momentum deficit (AMD) — a measure of their orbital excitation, etc.[4]

Here we adopt a reference case from the W11e/20M model (job #35) that produced a particularly good match to the terrestrial planets (Figs. 1 and 2). Venus, Earth and Mars formed in this simulation with nearly correct masses and semimajor axis: model mass $1.017\,M_{\text{Earth}}$ and $a = 0.727$ au for Venus ($0.815\,M_{\text{Earth}}$ and $a = 0.723$ au), $1.083\,M_{\text{Earth}}$ and $a = 1.034$ au for Earth ($1\,M_{\text{Earth}}$ and $a = 1$ au), $0.116\,M_{\text{Earth}}$ and $a = 1.525$ au for Mars ($0.107\,M_{\text{Earth}}$ and $a = 1.524$ au), where the numbers in parentheses list the real values for reference. The Mercury analog ended up to be too massive, which is related to the relatively large initial mass of protoplanets in W11e/20M and the assumption of inelastic mergers in Nesvorný et al. (2021a). The model orbits of Venus and Earth were only slightly less excited than in reality. The model orbit of Mars had a nearly perfect inclination (mean $i = 4.5°$ vs. real mean $i = 4.4°$) and somewhat lower eccentricity (mean $e = 0.028$ vs. real mean $e = 0.069$). The orbital structure of the asteroid belt was reproduced.

An interesting feature of the case highlighted here is related to the Earth's accretion history and the Moon-forming impact (Fig. 3). The initial growth of proto-Earth was fast. After accreting several Mars-class protoplanets, the proto-Earth reached mass $\simeq 0.52\,M_{\text{Earth}}$ by $t = 3$ Myr after the gas disk removal. A prolonged stage of planetesimal accretion followed during which the proto-Earth modestly grew to $\simeq 0.57\,M_{\text{Earth}}$ by $t \simeq 40$ Myr. Then, at $t = 41.3$ Myr, an accretional collision between two roughly equal-mass protoplanets occurred, and the Earth mass shot up to $\simeq 1.05\,M_{\text{Earth}}$. For comparison, Venus grew to 85% of its final mass in only ~ 3 Myr after the start of the simulation; the remaining 15% of mass was supplied to Venus by planetesimals over an extended time interval (~ 100 Myr). This supports the model of Jacobson et al. (2017), who argued that Venus has not developed a persistent magnetic field because it did not experience any late energetic impacts that would mechanically stir the core and create a long-lasting dynamo.

The accretional growth of the Earth shown in Fig. 3 would satisfy constraints from the Hf-W and U-Pb isotope systematics, assuming that the degree of metal-silicate equilibration was intermediate between the full and 40% equilibration considered in Kleine and Walker (2017); their Fig. 8. For example, Thiemens et al. (2019) found that the ^{182}W excess in lunar samples can be fully explained by the decay of now-extinct ^{182}Hf, and suggested that the Moon formed ~ 40–60 Myr after

---

[2] Mars represents only $\simeq 11\%$ of Earth's mass. Many terrestrial planet formation models suggest that a more massive planet should form at 1.2–1.8 au. This is called the small Mars problem.

[3] Meaning that the initial planetary embryos must have been about the mass of Mars.

[4] We found that in about 20% of cases, good Mars analogs formed (defined as planets with mass $0.5 < M < 2\,M_{\text{Mars}}$ and $1.2 < a < 1.8$ au) *and* the Earth and Venus ended with approximately correct masses, orbital excitation and separation (see Nesvorný et al., 2021a, for how this was quantified).
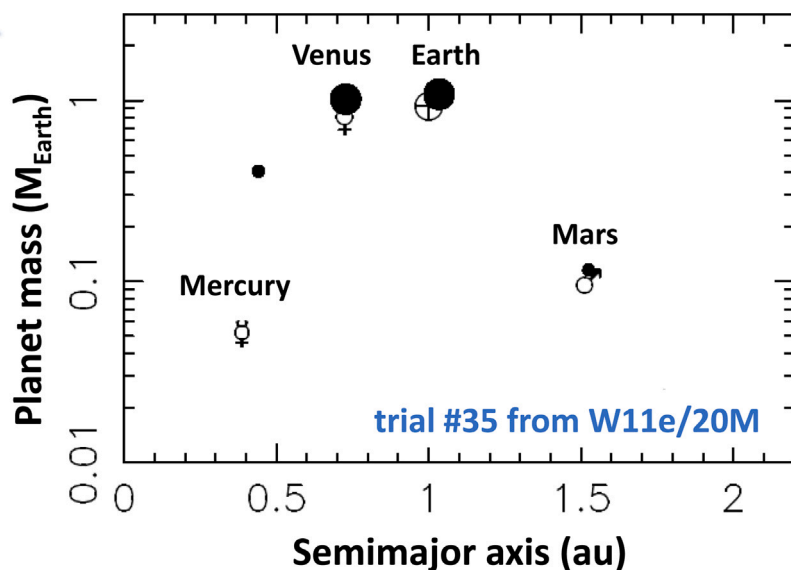
Fig. 1. The mass and radial distribution of terrestrial planets obtained in the best simulation of the W11e/20M model (Nesvorný et al., 2021a). The size of a dot is proportional to the planet mass. The real terrestrial planets are indicated by planetary symbols. The simulation failed to reproduce the correct mass of Mercury, but this is not a major limitation for the present study where we are interested in the impact histories of Venus, Earth, Mars, and the Moon.

the first solar system solids.[5] The low speed collision (the impact-to-escape speed ratio $v_{imp}/v_{esc} = 1.01$) between two nearly equal-mass protoplanets (the impactor-to-total mass ratio $\Gamma = 0.46$) falls into the preferred regime of Moon-forming impacts investigated in Canup (2012). In particular, the collision of two protoplanets with $\Gamma > 0.4$ would lead to the Moon formation from a well mixed disk and would therefore imply matching oxygen-isotope compositions of the Earth and Moon (Canup et al., 2021; but see Nakajima and Stevenson, 2014).

3. Chronology of lunar impacts

The radiometric ages, crater counts, and size distribution extrapolations are the basis of empirical models for impact cratering in the inner solar system (Neukum and Ivanov, 1994; Neukum et al., 2001; Hartmann and Neukum, 2001; Marchi et al., 2009; Hiesinger et al., 2012, 2020; Robbins, 2014; Marchi, 2021). On young lunar surfaces ($T \lesssim 100$ Ma; e.g., Cone, North/South Ray, Tycho; Hiesinger et al., 2016), where there is a good statistic only for very small, $D \ll 1$ km craters, the crater counts can be extrapolated up with some assumed size distribution. The size distribution can be patched together from crater counts on different terrains, which implicitly assumes that the size distribution does not change with time, or related — via the crater scaling laws — to observations of near-Earth asteroids (NEAs; Marchi et al., 2009). The goal is to establish the chronology function, $N_1(T)$, defined as the number of $D > 1$ km craters per km^2 (or 10^6 km^2; crater density) in an area with the crater accumulation age T.[6]

There are almost no radiometric data for lunar terrains with intermediate ages ($1 < T < 3$ Ga; but see Li et al., 2021), which makes it difficult to establish whether the impact flux on the Moon was essentially constant for $T < 3$ Ga, or whether it gradually declined from $T = 3$ Ga to the present epoch (Hartmann et al., 2007). An independent work indicates that the impact flux may have increased by a factor of $\sim$ 2–3 in the last $\sim$ 500 Myr (Culler et al., 2000; Mazrouei et al.,

2019; also see Kirchoff et al., 2021). Zellner and Delano (2015) and Huang et al. (2018), however, demonstrated through sample analyses and numerical modeling that the reported increase in the lunar impact spherule record (Culler et al., 2000) is a result of sample bias. The evidence for the impact flux increase is therefore less clear.

For old lunar surfaces ($T > 3$ Ga) with known radiometric ages (e.g., lunar maria, Fra Mauro/Imbrium highlands), the counts were traditionally done for large craters ($D > 1$ km), and these counts were then extrapolated down to estimate $N_1(T)$. In this sense, N_1 establishes a common reference for young and old lunar terrains. To relieve some of the uncertainties arising from the extrapolation method, the crater counts on some selected terrains (e.g., Orientale) were performed down to $D \simeq 1$ km, and used as a benchmark (Neukum and Ivanov, 1994).[7]

The radiometric ages have been measured for Apollo, Luna and Chang'e samples, and for lunar meteorites (Stöffler and Ryder, 2001; Li et al., 2021). The main difficulty in interpreting these ages — in terms of the cratering and geological processes occurring on the Moon — is how to relate different samples to different events. For example, we know that major, basin-forming impacts were happening before 4 Ga (e.g., at $T \simeq 4.21$ and 4.34 Ga; (Pidgeon et al., 2010; Grange et al., 2013; Merle et al., 2013; Norman et al., 2015), but we do not know which specific basins formed at that time. We therefore cannot empirically determine $N_1(T)$ for $T > 4$ Ga, at least not with the existing data.

The Imbrium-basin formation has a strong presence in many collected samples. According to the most accurate U-Pb geochronological measurements, the Imbrium basin formed at $T \simeq 3.92$ Ga (Zhang et al., 2019). The radiometric ages of lunar maria range between 3.1–3.7 Ga (Stöffler and Ryder, 2001). The crater counts for Fra Mauro/Imbrium highlands establish that $N_1(T)$ was about a factor of $\sim$ 10 higher at $T \simeq 3.92$ Ga than during the formation of most lunar maria ($T \simeq 3.1$–3.4 Ga; Robbins, 2014). There clearly was a substantial increase in the lunar cratering rate at $T \sim 3.5$ Ga.

The basic assumption of many empirical models for impact cratering is that the accumulated number of craters larger than D since time T, $N(D,T)$, is a separable function of D and T; i.e., $N(D,T) = N(D)N_1(T)$, where $N(D)$ is the cumulative size distribution of craters (per surface

---

[5] Note that $t = 0$ in the simulation time corresponds to the time of the protoplanetary gas dispersal some $\sim$ 3–10 Myr after the first solar system solids (Williams and Cieza, 2011), and the simulation time $t = 41.3$ Myr is thus roughly 44–51 Myr after the first solids.

[6] We use the notation where t runs forward in time and T is measured looking back from today. Time $t = 0$ roughly corresponds to the formation of first solar system solids $T \simeq 4.57$ Ga (Williams and Cieza, 2011).

[7] Several studies have concluded that secondary craters are unimportant for the $\sim$ km-scale lunar crater population (see (Bierhaus et al., 2018) for a review).
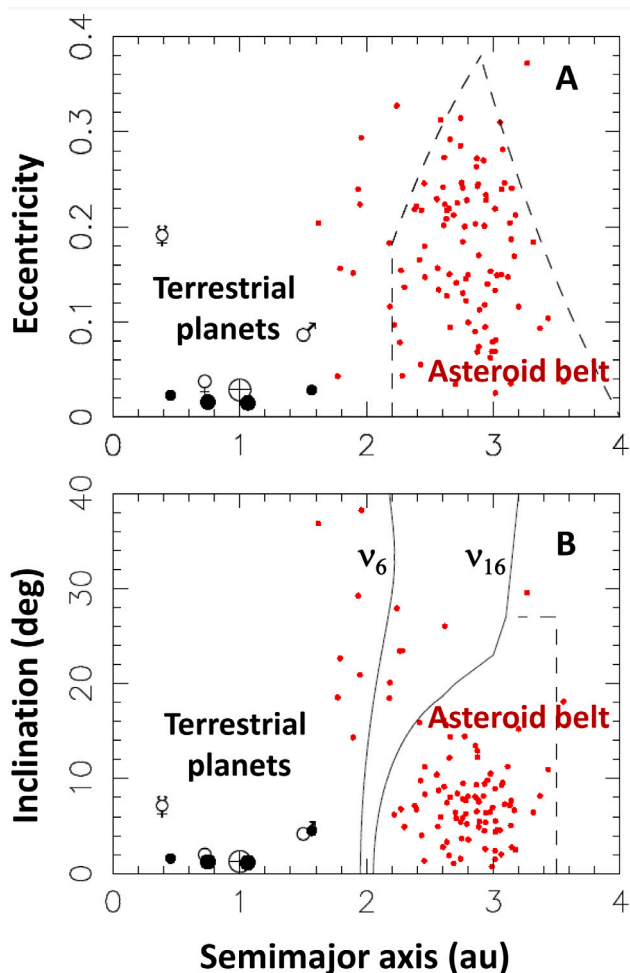
Fig. 2. The mean orbital elements of planets (black dots) and asteroids (red dots) produced in the best simulation of the W11e/20M model (Nesvorný et al., 2021a). The lines approximately carve out the asteroid belt region. The dashed lines correspond to $a = 2.2$ au, $q = a(1 - e) = 1.8$ au, and $Q = a(1 + e) = 4$ au in panel **A**, and $a = 3.5$ au and $i = 25°$ in panel **B**. The solid lines in **B** are the ν_6 and ν_{16} secular resonances (plotted here for $e \sim 0$). The mean orbits of the real terrestrial planets are indicated by planetary symbols. The simulation failed to reproduce the excited orbit of Mercury. (For interpretation of the references to color in this figure legend, the reader is referred to the web version of this article.)

area), the so-called *production function*, and $N_1(T)$ is the *chronology function*. Neukum and Ivanov (1994) approximated the production function by a polynomial (Eq. (2) and Table 1 in Neukum et al., 2001). Based on extrapolations with this polynomial, the N_1 chronology function was given as

$$N_1(T) = a[\exp(bT) - 1] + cT \tag{1}$$

with $a = 5.44 \times 10^{-14}$ km^{-2}, $b = 6.93$ Gyr^{-1}, and $c = 8.38 \times 10^{-4}$ Gyr^{-1} km^{-2}. Other published chronology functions used Eq. (1) with different coefficients. Marchi et al. (2009) constructed a production function based on the size distribution of NEAs and used it to determine $a = 1.23 \times 10^{-15}$ km^{-2}, $b = 7.85$ Gyr^{-1}, and $c = 1.30 \times 10^{-3}$ Gyr^{-1} km^{-2}. Hartmann et al. (2007) added a quadratic term to Eq. (1) to express a slow (linear) decline of the impact rate over the last ~ 3 Gyr.

At least some of the differences between different works must arise from different choices of the terrains where craters were counted and/or the size range of craters for which the counts were performed. Robbins (2014), for example, carefully carved their terrains of interest around the Apollo and Luna landing sites, and performed new crater counts for $D \gtrsim 1$ km craters. This has a notable advantage over the

previous results because N_1 is directly established from the counts themselves (no size extrapolation needed). For the oldest sites, however, the crater densities for $D \sim 1$ km may be affected by crater saturation (Robbins, 2014).

Fassett et al. (2012) used topography from the Lunar Orbiter Laser Altimeter (LOLA) on the Lunar Reconnaissance Orbiter (LRO) to measure the superposed impact crater distributions for 30 lunar basins. They reported their counts in terms of $N_{20}(T)$ — the same as $N_1(T)$ but for $D > 20$ km craters. For the Imbrium basin, Fassett et al. (2012) measured $N_{20} = 30 \pm 5$ (per 10^6 km^2) (later revised to $N_{20} = 26 \pm 5$ in Orgel et al., 2018). This is an important anchor of $N_{20}(T)$ for a $T \simeq 3.92$–Gyr old lunar terrain (Zhang et al., 2019).

4. Modeling the impact flux in the inner solar system

There are at least three major source populations of impactors in the inner solar system: (i) leftover planetesimals in the terrestrial planet zone (0.3–1.75 au), (ii) main-belt asteroids (1.75–4 au; the range given here includes the Extended belt or E-belt for short, (Bottke et al., 2012)),[8] and (iii) comets. Here we first discuss the results for (ii) and (iii) that were taken from previous work (Sections 4.1 and 4.2). The model for leftover planetesimals is described in Section 4.3.

4.1. Asteroids

In Nesvorný et al. (2017a), we published a dynamical model for asteroid impactors. The model used the same setup for the radial migration and instability of the outer planets as the terrestrial planet formation model described in Section 2 (the instability happens at $t = 5.8$ Myr after the gas disk dispersal). To start with, the terrestrial planets were placed on the low-eccentricity and low-inclination orbits. The surface density profile of asteroids was assumed to follow $\Sigma(r) \propto r^{-1}$. The radial profile was smoothly extended from $r > 2$ au, where the model can be calibrated on observations of main belt asteroids (see below), to $r = 1.75$–2 au. This fixed the initial number of bodies in the now largely extinct E-belt (Bottke et al., 2012). The results had large statistics (50,000 model asteroids) and full temporal coverage (integration time $t = 0$–4.57 Gyr).

The flux of asteroid impactors was calibrated from today's asteroid belt. We showed that the model distribution at the simulated time $t = 4.57$ Gyr (i.e., at the present epoch) was a good match to the orbital distribution of asteroids. The number of model $d > 10$ km asteroids at $t = 4.57$ Gyr was set to be equal to the number of $d > 10$ km main-belt asteroids ($\simeq 8200$), as measured by Wide-field Infrared Survey Explorer (WISE; Mainzer et al., 2019). When propagated backward in time — using the simulation results — this provided the number of asteroids and asteroid impactors over the whole solar system history.

The size distribution of main-belt asteroids was used to set up the model size distribution. The size distribution is relatively steep for $d \simeq 10$–15 km (the cumulative power index $\gamma \simeq -2$), flattens for $d = 30$–50 km ($\gamma \simeq -1$), and becomes much steeper for $d > 100$ km ($\gamma \simeq -3$). The adopted size distribution allowed us to scale the absolutely calibrated results for $d > 10$ km impactors to any impactor size. For example, there are $\simeq 3.5$ times fewer impactors with $d > 20$ km, $\simeq 8.9$ times fewer impactors with $d > 50$ km, and $\simeq 26$ times fewer impactors with $d > 100$ km. The collisional evolution of asteroids during the early epochs was not accounted for in the model (see Nesvorný et al., 2017a, for a discussion); here we are mainly interested in the lunar crater record that likely does not reach back to these early stages (Section 8).

---

[8] The E-belt, representing the inner extension of the main asteroid belt at 1.75–2 au, was hypothesized by Bottke et al. (2012) to be an important source of terrestrial and lunar impactors. There are presently no asteroids in this region except for Hungarias with $i = 15°$–30°. The E-belt population on low-inclination orbits was presumably cleared during the giant planet migration/instability.
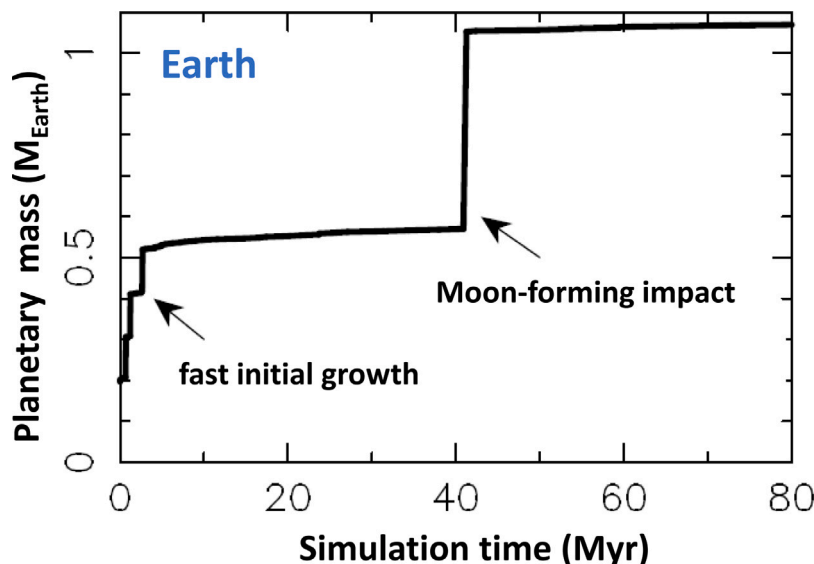
Fig. 3. The accretional growth of the Earth in the best case from the W11e/20M model (Nesvorný et al., 2021a). The Moon-forming collision between two roughly equal-mass bodies occurred at $t = 41.3$ Myr in this simulation.

Nesvorný et al. (2017a) empirically approximated the impact profiles by a sum of three exponential functions, each with a different *e*-folding time. Here we find a simpler functional form with fewer parameters that approximates the asteroid impact flux equally well. In terms of the cumulative number of Earth impactors with diameters $> d$ at times $> t$, the new chronology function is

$$F(d,t) = F_1(d)\exp[-(t/\tau)^{\alpha}] + F_2(d)T \ , \tag{2}$$

with $\tau = 65$ Myr, $\alpha = 0.6$, $T = 4570 - t$ and t in Myr. This expression should not be used for $t \sim 0$, because Eq. (2) does not take into account the effects of early collisional grinding.

The first term in Eq. (2) accounts for the dynamical decline of asteroid impactors during early epochs. The second term represents the constant impact flux in the last 3 Gyr. There are two size-dependent factors in Eq. (2). $F_1(d)$ follows the size distribution of main-belt asteroids (Bottke et al., 2005); the fit to simulation results gives $F_1(10\,\text{km}) = 225$. We use the factors mentioned above to scale the impact flux to any $10 \leq d \leq 100$ km. Also, from the main belt size distribution, $F_1(1\,\text{km}) = 3.0 \times 10^4$ (Section 10). $F_2(d)$ is calibrated on modern NEAs. Nesvorný et al. (2021a) estimated ~ 3 impacts of $d > 10$ km NEAs on the Earth per Gyr; we thus have $F_2(10\,\text{km}) = 3 \times 10^{-3}$ Myr^{-1}. Harris and D'Abramo (2015) and Morbidelli et al. (2020) estimated that $d > 1$ km NEAs impact on the Earth on average every 0.75 Myr; we thus have $F_2(1\,\text{km}) = 1.3$ Myr^{-1}.

This fully defines the historical impact flux of asteroids on the Earth. We use the results of Nesvorný et al. (2017a) to obtain the impact flux for other terrestrial worlds as well. For the case considered here, Venus received $\simeq 1.2$ times more impacts than the Earth, Mars received $\simeq 2.9$ times fewer impacts, and the Moon received $\simeq 20$ times fewer impacts (Mercury is not considered in this work). The overall Mars-to-Moon ratio in the number of asteroid impacts is $\simeq 7$ (dominated by early impacts; see Section 13 for Mars). For reference, Nesvorný et al. (0000) reported the Mars-to-Moon ratio of ~ 7.5 from modeling impacts of large (modern) NEAs. We use these factors to re-scale the impact flux from the Earth to Venus, Mars and the Moon. This is an excellent approximation of the modeling results obtained in Nesvorný et al. (2017a). The mean impact speeds of asteroids on Venus, Earth, Mars and the Moon are 28.6, 23.5, 13.7, and 21.4 km s^{-1}, respectively (gravitational focusing included).

Fig. 4 shows the historical impact flux of asteroids on the terrestrial worlds. Most impacts happened early: for example, $\simeq 90\%$ of impacts

happened in the first 400 Myr. There were $\simeq 239$ $d > 10$ km asteroid impacts on the Earth over the whole history of the solar system, $\simeq 118$ $d > 10$ km impacts for $t > 42$ Myr (after the Moon formation in the case considered here), and $\simeq 16$ $d > 10$ km impacts for $t > 650$ Myr (post-Imbrium). These fluxes imply, via the scaling factors mentioned above, only $118/3.5/20 \sim 1.7d > 20$ km (i.e., basin-scale) impacts on the Moon for $t > 42$ Myr. This implies that the asteroid contribution to lunar basin record was insignificant.[9] We discuss this issue in detail in Section 8.

4.2. Comets

A model for cometary impactors was developed in Nesvorný et al. (2017b). To start with, a million cometesimals were distributed in a disk beyond Neptune, with Neptune on an initial orbit at 23 au. The bodies were given low orbital eccentricities, low inclinations, and the surface density $\Sigma(r) \propto r^{-1}$. The disk was truncated at 30 au to assure that Neptune stopped migrating near its current orbital radius at $\simeq 30$ au (Gomes et al., 2004). The simulations were run from $t = 0$ (approximately the gas disk dispersal) to the present epoch ($t \simeq 4.57$ Gyr). The effects of outer planet (early) migration/instability, galactic tides, and perturbations from passing stars were accounted for in the model. The results were shown to be consistent with the orbital distribution of modern comets, Centaurs and the Kuiper belt (Nesvorný et al., 2017b, 2019, 2020; Vokrouhlický et al., 2019).

The size distribution of outer disk cometesimals was calibrated from the number of large comets observed today, the number of $d > 10$ km Centaurs detected by OSSOS (Nesvorný et al., 2019), the size distributions of Jupiter Trojans and KBOs, and from the general condition that the initial setup leads to plausible migration/instability histories of the outer planets (see Nesvorný, 2018 for a review). The calibration gives $\sim 6 \times 10^9$ $d > 10$ km and $\sim 5 \times 10^7$ $d > 100$ km cometesimals in the original disk. The size distribution is expected to closely follow a power law with the cumulative index $\gamma \simeq -2.1$ for $10 < d < 100$ km

---

[9] While this is true in the model presented here, where the asteroid depletion is relatively modest ($\lesssim 90\%$; Nesvorný et al., 2017a also see Roig and Nesvorný, 2015; Deienno et al., 2018), it has to be pointed out that some dynamical models imply much larger depletion ($> 90\%$, e.g., Clement et al., 2019). The asteroid contribution to the lunar basin record would presumably be more significant in these models.
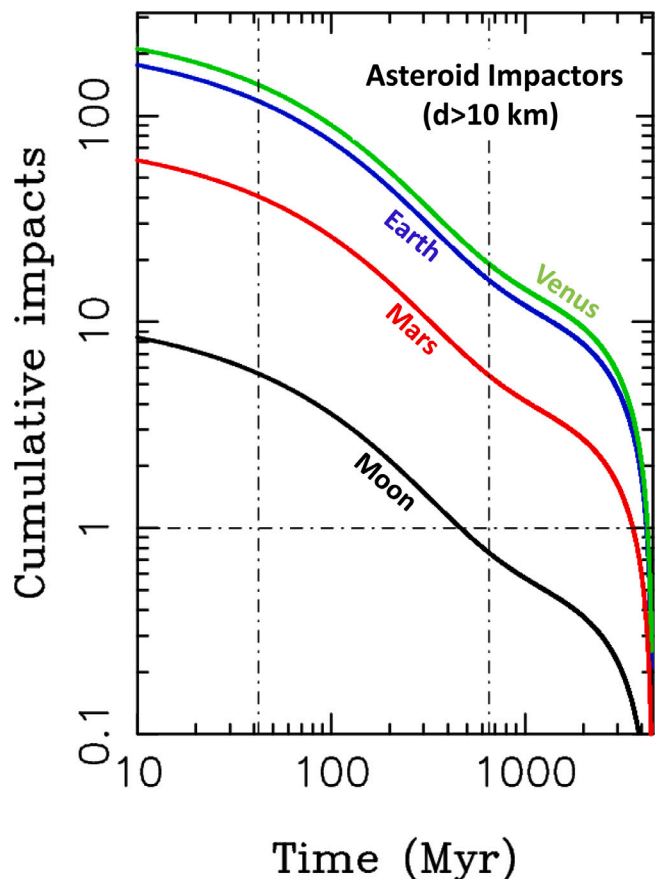
Fig. 4. The impact flux of $d > 10$ km asteroids on the Moon (black line), Earth (blue), Venus (green), and Mars (red). The plot shows the accumulated number of impacts *since* time t (i.e., on the surface with age T), where $t = 0$ ($T = 4.57$ Ga) is the birth of the solar system, and $t \simeq 4.57$ Gyr ($T = 0$) is the present time. This is an analytic fit (Eq. (2)) to the simulation results of Nesvorný et al. (2017a). The vertical dash-dotted lines show $t = 42$ Myr and $t = 650$ Myr for reference. (For interpretation of the references to color in this figure legend, the reader is referred to the web version of this article.)
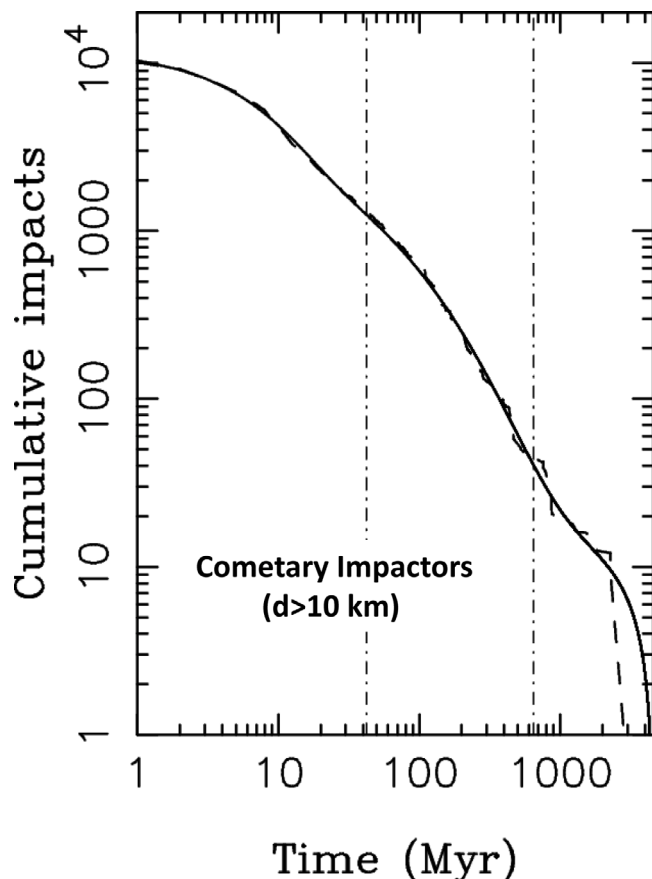

Fig. 5. The impact flux of $d > 10$ km comets on the Earth. The impact profile shown by the dashed line was obtained from the model results in Nesvorný et al. (2017b). The solid line shows the analytic fit given in Eq. (3). The fits for Venus and Mars are equally good. Disregarding comet disruptions, we estimate that ~ 4 impacts of $d > 10$ km comets would happen on the Earth in the last Gyr. The vertical dash-dotted lines show $t = 42$ Myr and $t = 650$ Myr for reference.

(Morbidelli et al., 2009b), and have a transition to a much steeper slope for $d > 100$ km (Bernstein et al., 2004; Fraser et al., 2014). The distribution is a product of the initial size distribution that was modified by collisional grinding (Nesvorný and Vokrouhlický, 2019).

The impact flux of comets on the terrestrial worlds was computed with the Öpik algorithm (Bottke et al., 1994; there were not enough planetary impacts recorded by the integrator to obtain the flux directly from the impact statistics). The results of the Öpik code were normalized to the initial number of comets in the original disk (see above). The calibrated model gives us the flux of cometary impactors over the whole history of the solar system. In total, over 4.57 Gyr, there were $\simeq 10^4$ impacts of $d > 10$ km comets on the Earth (Fig. 5). The great majority of cometary impacts happened early. For example, 90% of impacts happened in the first $\simeq 55$ Myr, and 99% of impacts happened in the first $\simeq 370$ Myr. The wavy decline of cometary impacts is related to the dispersal of the outer cometesimal disk, which was an important source of impactors during the early epochs, and the slower decay of the scattered disk population, which is the main source of modern comets.

An excellent approximation of the cumulative impact flux of comets on the Earth is

$$F(d,t) = C_s(d) \left\{ F_1 \exp[-(t/\tau_1)^{\alpha_1}] + F_2 \exp[-(t/\tau_2)^{\alpha_2}] + F_3(4570 - t) \right\},$$

(3)

with $F_1 = F_2 = 6.5 \times 10^3$, $\tau_1 = 7$ Myr, $\alpha_1 = 1$, $\tau_2 = 13$ Myr, $\alpha_2 = 0.44$, $F_3 = 4 \times 10^{-3}$ Myr^{-1}, $C_s(d) = 1$ for $d = 10$ km, and t in Myr (Fig. 5). This expression should not be used for $t \sim 0$, because Eq. (3) does not take into account the effects of early collisional grinding.

The impact profile in Eq. (3) is anchored to the impact rate of comets at the present epoch. We find, using the calibration discussed above, that ~ 4 $d > 10$ km comets should have impacted on the Earth in the last Gyr;[10] the average time interval between cometary impacts is ~ 250 Myr (this ignores comet disruption; see below). For comparison, the same method yields $\sim 44{,}000$ yr as the average interval between $d > 10$ km impacts on Jupiter. Scaling this down with $\gamma = -2.1$, we estimate that $d > 1$ km comets impact Jupiter on average every ~ 350 yr. This is within the range of historical record of impacts on (and close encounters to) Jupiter (Zahnle et al., 2003; Dones et al., 2009). Venus receives $\simeq 0.94$ times the number of Earth impacts,[11] Mars $\simeq 5.0$ times fewer, and the Moon $\simeq 17$ times fewer. This gives the Mars-to-Moon ratio of cometary impacts $\simeq 3.4$. The mean impact speeds of comets are higher than those of asteroid impactors: 28.2 km s^{-1} for the Earth,

---

[10] This would be comparable to the current impact flux of asteroids (Nesvorný et al., 2021b). If comet disruptions are accounted for, however, the impact flux of $d > 10$ km comets on the Earth is reduced by a factor of ~ 6, a factor of few below the asteroid flux.

[11] There are more comets with perihelion distances $q \lesssim 1$ au than with $q \lesssim 0.7$ au, and this leads to a slight preference for Earth impacts over Venus impacts.

25.5 km s^{-1} for the Moon, 36.8 km s^{-1} for Venus, and 19.7 km s^{-1} for Mars (focusing included).

The physical lifetime of comets is shorter than their dynamical lifetime (Levison and Duncan, 1997; Levison et al., 2002), partly because comets become active and lose mass, but mainly because they spontaneously disrupt (Chen and Jewitt, 1994; Levison et al., 2006; Di Sisto et al., 2009). The exact mechanism behind the observed comet disruptions is unknown but rotational spin-up, thermal stresses and volatile-driven outbursts are all expected to contribute. In Nesvorný et al. (2017b), we tested several disruption laws and found that they produce comparable results. In the simplest of these models, the physical lifetime of comets is limited to a fixed number of perihelion passages $N_p(q)$ below q. To fit the orbital inclination distribution of observed $d \sim 1$ km comets, we found $N_p(q) \sim 500$ for $q = 2.5$ au. The physical lifetime is expected to increase with comet size. To explain the observed number of $d > 10$ km Jupiter-family comets, $N_p(2.5) \sim 5{,}000$ is needed for $d = 10$ km. This hints on a roughly linear dependence of $N_p(2.5)$ on size, $N_p(2.5) \sim 500 \times (d/1\,\mathrm{km})$, and $N_p(2.5) \sim 50{,}000$ for $d = 100$ km.

The impact flux of comets on the terrestrial worlds is reduced, relative to the expectations discussed above, if spontaneous comet disruptions are taken into account. We include comet disruption, using the approximate linear dependence described above, in the Öpik calculation of the impact flux. The impact flux of comets on the Earth is reduced by a factor of ~ 59 for $d > 1$ km, ~ 6 for $d > 10$ km, and ~ 1.8 for $d > 100$ km. The reduction factors for Venus and the Moon are similar. The reduction factors for Mars are slightly lower, 36, 4.9, and 1.7, respectively. We account for these factors in Fig. 6. The total number of $d > 10$ km comet impacts on the Earth is reduced to $\sim 1{,}700$, of which ~ 200 happen for $t > 42$ Myr, and ~ 6 happen for $t > 650$ Myr. The Moon is expected to receive ~ 12 $d > 10$ km comet impacts after its formation (assumed here to happen at $t \sim 42$ Myr with the instability at $t \lesssim 10$ Myr). This is a factor of ~ 17 below what would be needed to explain ~ 200 $D > 150$ km lunar craters (Bottke and Norman, 2017; a $d = 10$ km impactor is assumed here to produce a $D = 150$ km lunar crater). A more powerful source of lunar impactors is clearly needed.

4.3. Leftover planetesimals

4.3.1. N-body simulation setup

We are interested in the impact flux on the terrestrial worlds after the Moon-forming impact, $t > 41.3$ Myr in the case described in Section 2. With this goal in mind we recorded the orbits of planets and planetesimals in the original simulation at $t = 42$ Myr (i.e., shortly after the Moon-forming impact). The planetesimals in the asteroid belt region were ignored (see below and Section 4.1 for asteroids). Given that Mercury was too massive in the original simulation (Section 2), which could cause problems when examining the impact flux, we ignored Mercury in the follow-up simulations. All other planets, Venus to Neptune were included. We assumed that the terrestrial worlds were fully grown at $t = 42$ Myr and their masses did not subsequently change. The orbits of planets $t = 42$ Myr were taken from the original simulation (i.e., were *not* reset to the real orbits of the terrestrial planets).

To increase the model statistics, each planetesimal was cloned thousand times by slightly altering the velocity vector ($< 10^{-6}$ fractional change). In total, we thus had 128,000 planetesimal clones at $t = 42$ Myr. The N-body integrator known as `swift_rmvs4` (Levison and Duncan, 1994), which is an efficient implementation of the Wisdom–Holman map (Wisdom and Holman, 1991), was used to follow the system of planets and (massless) planetesimals over 1 Gyr. The simulation was split over 1280 Ivy-Bridge cores of the NASA Pleiades Supercomputer. All impacts of planetesimals on planets were recorded by the N-body integrator.

In the model considered here, planetesimals were originally distributed with a flat radial profile, $\Sigma(r) \propto r^{-1}$, from 0.3 to 4 au (Section 2). The inner part of the planetesimal disk, $r < 1.5$ au, contained the initial mass $\simeq 0.65\,M_{\mathrm{Earth}}$. This may or may not correctly
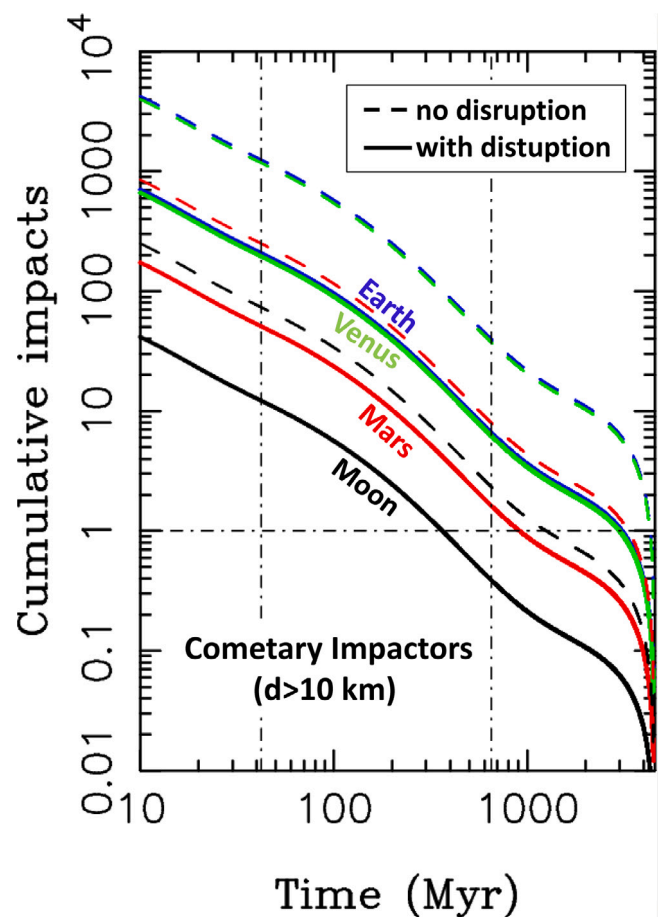

Fig. 6. The impact flux of $d > 10$ km comets on the Moon (black line), Earth (blue), Venus (green), and Mars (red). The dashed lines show the analytic fits from Eq. (3) disregarding comet disruptions. The solid lines show the impact flux when comet disruptions are accounted for. The vertical dash-dotted lines show $t = 42$ Myr and $t = 650$ Myr for reference. (For interpretation of the references to color in this figure legend, the reader is referred to the web version of this article.)

approximate the physical conditions that existed in the inner solar system at $t = 0$ (the time of gas disk dispersal). We developed a weighting scheme to test implications of different assumptions for the impact flux. Each planetesimal was assigned a weight, $0 \leq w \leq 1$, depending on its starting orbit and the adopted surface density profile. For example, to test the effects of the planetesimal disk truncation at some outer radius, r_{out}, the planetesimals with $r < r_{\mathrm{out}}$ at $t = 0$ were given weights $w = 1$, and the planetesimals with $r > r_{\mathrm{out}}$ were given weights $w = 0$. For each assumption, the impact record was constructed by monitoring the weights of impactors recorded by the N-body integrator.

4.3.2. Collisional evolution model

We used the `Boulder` code (Morbidelli et al., 2009a) to model the collisional evolution of planetesimals (Bottke et al., 2007). `Boulder` employs a statistical particle-in-the-box algorithm that is capable of simulating collisional fragmentation of planetesimal populations. It was developed along the lines of other published codes (e.g., Weidenschilling et al., 1997; Kenyon and Bromley, 2001). In brief, for a given impact between a projectile and a target body, the algorithm computes the specific impact energy Q, defined as the kinetic energy of the projectile divided by the total (projectile plus target) mass, and compares it with critical impact energy, Q_{D}^*, defined as the energy per unit mass needed to disrupt and disperse 50% of the target. For each

collision, the mass of the largest remnant is computed from the scaling law for monolithic basalt (e.g., Benz and Asphaug, 1999).

The main input parameters of the Boulder code are: the (i) initial size distribution of the simulated populations, (ii) intrinsic collision probability p_i, and (iii) mean impact speed v_i. The initial size distribution is discussed in Section 5. The probabilities $p_i(t)$ and velocities $v_i(t)$ of mutual collisions between planetesimals were computed from the terrestrial planet simulation described in Section 2. We used the Öpik algorithm (Bottke et al., 1994) and considered each pair of planetesimals at a time at each timestep. The results were averaged over all pairs (at each timestep) to give us a time-dependent description of the collisional environment. The leftover planetesimals were modeled as a single population in Boulder (e.g., we did not consider high-i or high-i orbits separately; simulations with the multi-annulus version of Boulder are left for future work). The collisional probabilities were initially high ($p_i \sim 10^{-16}$ km^{-2} yr^{-1} for $r_{out} = 1.5$ au and $t < 3$ Myr), and quickly decreased as the planetesimal population dynamically and collisionally declined (Sections 5 and 6). The impact speeds between planetesimals increased from $v_i \sim 10$ km s^{-1} at $t \lesssim 5$ Myr to $v_i \sim 20$ km s^{-1} later on. We implemented the impact speed dependence of Q_D^* from Leinhardt and Stewart (2012) (the disruption threshold shifts to higher specific energies when the impact speeds are higher).

5. Collisional evolution of planetesimals

The collisional evolution acted, along with the dynamical decay, to reduce the number of planetesimals in the terrestrial zone. We show below that the collisional grinding happened very early and produced convergence, where different (assumed) planetesimal populations at $t = 0$ evolved to similar populations by the time of the Moon-forming impact (both in the shape and overall normalization of the size distribution; Bottke et al., 2007). This result is used to approximately calibrate the number of leftover planetesimals and their impact profiles after Moon's formation.

We defined the total mass of leftover planetesimals at $t = 0$ (M_0) and $t = 42$ Myr (M_{42}), and performed collisional simulations with Boulder (Section 4.3.2) to understand the relationship between M_0 and M_{42} for different assumptions. Fig. 7 shows an example of Boulder run where we placed $M_0 = 1$ M_{Earth} in planetesimals at 0.5–1.5 au. The initial size distribution was assumed to be a broken power-law $N(>d) \propto d^{-\gamma}$ with $\gamma = 1.5$ for $d < d^*$ and $\gamma = 5$ for $d > d^*$, and $d^* \sim 100$ km. This setup was inspired by the streaming instability model of planetesimal formation (Youdin and Goodman, 2005), where the new-born planetesimals have the characteristic size $d \sim 100$ km, and the asteroid size distribution that shows a break at $d \simeq 100$ km (Morbidelli et al., 2009a). We do not consider very large, Ceres-class planetesimals that may have formed in the terrestrial planet zone, because the lunar impact record does not provide direct constraints on their population. According to our tests, however, energetic impacts on Ceres-class and larger objects produce fragments and this can influence the size distribution of planetesimals in the range relevant for the lunar impact record. Similarly, lunar impactors can be produced in collisions between protoplanets (Wishard et al., 2022). We leave these issues for future studies. The very large planetesimals may have also been important for the late delivery of highly siderophile elements (HSEs; Section 14) to the Earth (Bottke et al., 2010; Marchi et al., 2014) and Mars (Marchi et al., 2020).

The Boulder code was run from $t = 0$ to 1 Gyr. We found that the size distribution of planetesimals rapidly changed and reached an equilibrium shape by only $t \sim 20$ Myr. The subsequent collisional evolution was insignificant because the planetesimal population was reduced by a large factor (~ 100 by $t = 42$ Myr, collisional and dynamical removals combined). In this sense, the shape of the size distribution of leftover planetesimals at the time of the Moon-forming impact, and any time after that, is a fossilized imprint of the intense collisional grinding that happened in the first ~ 20 Myr (Bottke et al., 2007).
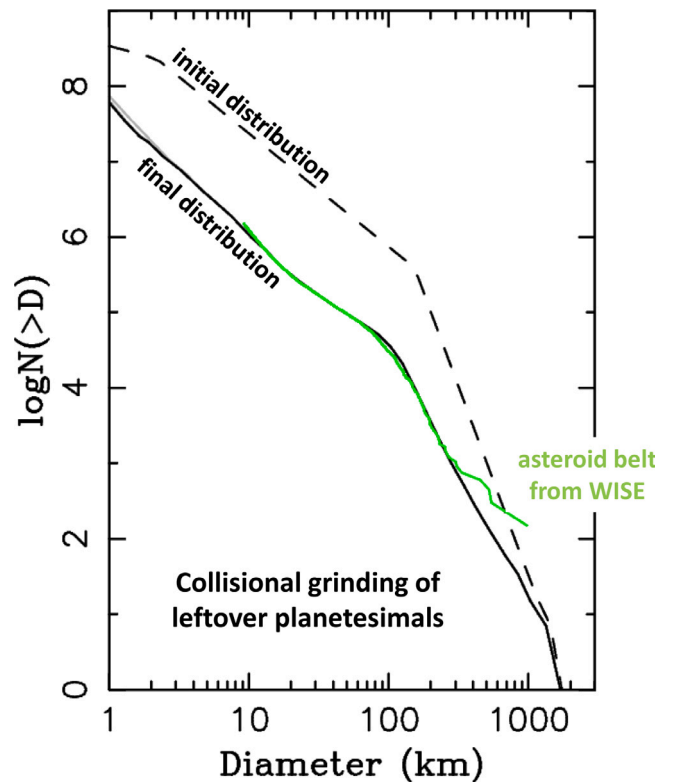

Fig. 7. The collisional evolution of leftover planetesimals. Initially, at $t = 0$, the planetesimal disk at 0.5–1.5 au was assumed to have the mass $M_0 = 1$ M_{Earth}, and a broken power-law distribution with a steeper slope for $d > 140$ km and a shallower slope for $d < 140$ km (dashed line). The black solid line shows the size distribution after 42 Myr of collisional grinding. The collisional evolution for $t > 42$ Myr is negligible. For reference, we also show the size distribution of the main asteroid belt from WISE (green line; Mainzer et al., 2019) that was vertically shifted to plot near the black solid line. (For interpretation of the references to color in this figure legend, the reader is referred to the web version of this article.)

The equilibrium size distribution shows a break at $d \simeq 100$ km, a shallow slope for $d = 20$–100 km, and a slightly steeper slope for $d < 20$ km. It is remarkably similar to that of the (scaled) asteroid belt (Fig. 7). This is an encouraging sign, because an asteroid-like size distribution is just what is needed to explain the size distribution of ancient lunar craters (Strom et al., 2005). Minton et al. (2015), however, pointed out that the main-belt-like size distribution of impactors would produce too many lunar basins. This could indicate that the size distribution of ancient impactors with $d \gtrsim 10$ km was slightly steeper than that of today's asteroid belt (Section 14).

The number of terrestrial planetesimals was strongly reduced by collisional grinding. With $M_0 = 1$ M_{Earth}, and the initial size distribution defined above, there were $\sim 1.9 \times 10^7$ $d > 10$ km, 6.7×10^6 $d > 20$ km, and 6.9×10^5 $d > 100$ km planetesimals at $t = 0$. By $t = 42$ Myr, the planetesimal population was reduced to $\sim 10^6$ $d > 10$ km, 2.6×10^5 $d > 20$ km, and 3.5×10^4 $d > 100$ km planetesimals (~ 19–26 reduction factors). The total mass of the planetesimal population dropped by a factor of ~ 19 to $M_{42} = 0.053$ M_{Earth}. The numbers quoted above only account for the effects of collisional grinding. In the dynamical simulations, the number of planetesimals was reduced by a factor of ~ 3.1 from $t = 0$ to 42 Myr. Combining the dynamical and collisional removals we therefore estimate the overall reduction of ~ 59–81, and $\sim 3.2 \times 10^5$ $d > 10$ km, 8.4×10^4 $d > 20$ km, and 1.1×10^4 $d > 100$ km planetesimals at $t = 42$ Myr.[12]

---

[12] An implicit assumption here is that the dynamical loss rate is independent of size.

The effects of collisional grinding depend on the initial mass M_0 (Bottke et al., 2007): stronger/weaker collisional grinding is expected if M_0 was higher/lower. We performed a large number of simulations with the Boulder code to characterize this dependence in detail. We found that the stronger grinding for larger initial masses leads to a situation where M_{42}, and the population leftover planetesimals at $t = 42$ Myr, do *not* sensitively depend on M_0; hence the aforementioned convergence. For $M_0 > 0.1\ M_{\text{Earth}}$, we estimate $\sim (2.6\text{--}5.2) \times 10^5\ d > 10$ km planetesimals at $t = 42$ Myr. The effects of collisional grinding are greatly reduced for $M_0 < 0.1\ M_{\text{Earth}}$, but the number of planetesimals at $t = 42$ Myr ends up to be smaller in this case (because it was already small initially). For $M_0 = 0.03\ M_{\text{Earth}}$, for example, we found $\sim 1.5 \times 10^5$ $d > 10$ km planetesimals at $t = 42$ Myr.

The results depend on other parameters as well, mainly on the shape of the initial size distribution and on the scaling law adopted in Boulder. Our choice of the initial size distribution described above puts most mass in $d \sim 100$ km planetesimals. It is possible that most mass was in smaller or larger planetesimals. If so, this would imply a smaller population of $d > 100$ km planetesimals at $t = 42$ Myr (Section 14). In the collisional simulations described above, we adopted the standard disruption law for monolithic basalt (Benz and Asphaug, 1999). Scaling laws that significantly differ from Benz and Asphaug (1999) (e.g., for porous bodies) would presumably produce different results (but note that most important collisions happen in the gravity regime where the material strength is not that important).

6. Impact flux of leftover planetesimals

In total, in the simulation described in Section 4.3.1, there were 14,091 impacts of leftover planetesimals on Venus, 9,418 impacts on the Earth, and 2,292 impacts on Mars in 1 Gyr. This represents 11%, 7.4%, and 1.7% of the population of leftover planetesimals in the terrestrial planet zone at the time of the Moon-forming impact ($t = 42$ Myr). The number of planetesimal impacts on the Moon was obtained from the number of impacts on the Earth by re-scaling the results to the smaller cross-section and focusing factor of the Moon. This gives the Earth-to-Moon ratio of $\simeq 20$, and the overall lunar impact probability of $\simeq 0.4\%$. The impact probabilities are substantially higher than the ones obtained for asteroids ($\sim 1\%$ for Earth impacts from the inner main belt) and comets (1.6×10^{-6} for Earth impacts if comet disruption is ignored).

The raw impact profile — i.e., the (uncalibrated) impact profile where all planetesimals were given the same weight — is shown in Fig. 8. The initial impact flux decline is intermediate between those of asteroids and comets. Specifically, 90% of planetesimal impacts occur within 80 Myr (400 Myr for asteroids and 55 Myr for comets) and 99% of impacts occur within 300 Myr. The leftover planetesimals are therefore expected to produce a shorter tail of late impacts than asteroids. Compared to asteroids, however, the leftover planetesimals represented a much larger initial population and are therefore favored, by a large factor, to produce impacts for $t < 1$ Gyr (see below).

To a great accuracy, the profile shown in Fig. 8 can be approximated by a stretched exponential

$$F(d, t) = F(d) \exp[-(t/\tau)^\alpha]\,, \tag{4}$$

with $\tau = 12.2$ Myr and $\alpha = 0.5$. For comparison, Morbidelli et al. (2018) estimated $\tau = 10$ Myr and $\alpha = 0.5$. Our expression should not be used for $t < 10$ Myr, because Eq. (4) does not take into account the effects of early collisional grinding (Section 5). We assume that there were 4×10^5 $d > 10$ km planetesimals at $t = 42$ Myr (a factor of ~ 2 uncertainty; Section 5) and use this number to absolutely calibrate of the impact flux for $t > 42$ Myr. To scale the results to larger impactors, given the results shown in Fig. 7, we adopt the asteroid belt size distribution as a reference. This gives $F(d) = 1.8 \times 10^5$ for $d = 10$ km, $F(d) = 5.1 \times 10^4$ for $d = 20$ km, and $F(d) = 6.9 \times 10^3$ for $d = 100$ km.
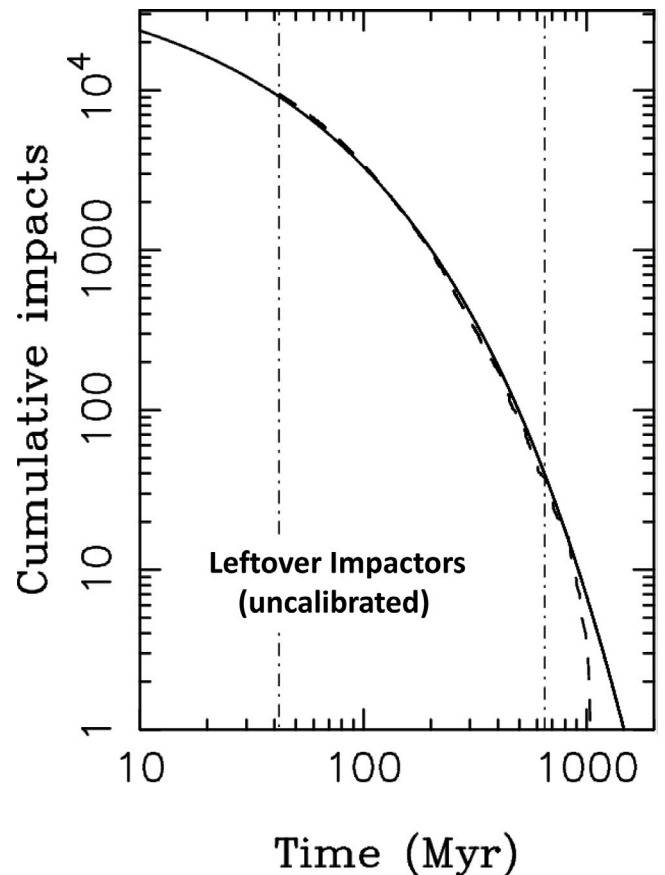

Fig. 8. The (uncalibrated) impact flux of leftover planetesimals on the Earth. The dashed line is the profile for all impacts on the Earth, 9,418 in total, recorded in the simulation after the Moon-forming impact ($t > 42$ Myr). The solid line shows the analytic fit given in Eq. (4). The model profile drops more steeply for $t = 0.8\text{--}1$ Gyr than the analytic fit, because the simulation ended at $t = 1$ Gyr, and no impacts were recorded for $t > 1$ Gyr. The vertical dash-dotted lines show $t = 42$ Myr and $t = 650$ Myr for reference.

Similar results were obtained for Venus and Mars. The functional form in Eq. (4) provides an excellent approximation for Venus ($F(d) = 2.5 \times 10^5$ for $d = 10$ km — Venus receives $\simeq 1.4$ times the number of Earth impacts). The same holds for Mars ($F(d) = 4.4 \times 10^4$ for $d = 10$ km — Mars receives 4.1 times fewer impacts than the Earth). For Mars, however, $\tau = 13.5$ Myr fits the model profile better than $\tau = 12.2$ Myr. This indicates that the decline of Mars impactors was slightly slower, presumably because the planetesimals with $r \sim 1.5$ au had longer dynamical lifetimes than the ones below 1 au (e.g., Deienno et al., 2019). For the Moon, we adopt the Earth impact profile and scale it down by a factor of $\simeq 20$.

7. Dependence on the initial radial profile

The initial surface density profile, $\Sigma(r)$, of planetesimals in the inner solar system is unknown. The relatively low mass of the main asteroid belt ($\simeq 4.5 \times 10^{-4}\ M_{\text{Earth}}$; DeMeo and Carry, 2013) probably suggests that the initial planetesimal mass at $r \simeq 2\text{--}4$ au was low (see Raymond and Nesvorny, 2020 for a review). In the standard model of the terrestrial planet formation (Section 2), the initial planetesimal mass in the terrestrial planet region ($r < 1.5$ au) is usually assumed to be $M_0 > 0.1\ M_{\text{Earth}}$ (we adopted this assumption to calibrate the impact model in Section 6). How the profile changed from the high surface density at $r \sim 1$ au to the low surface density at $r > 2$ au is uncertain.

To fix the initial number of asteroids in the E-belt ($r = 1.75\text{--}2$ au), we adopted $\Sigma \propto r^{-1}$ for $r > 1.75$ au, and used the main belt
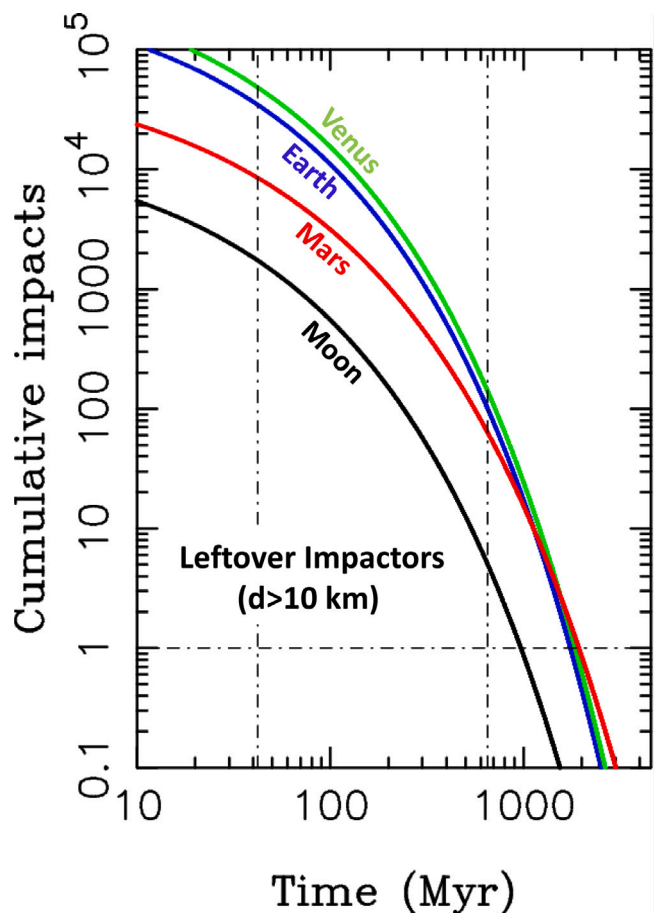
Fig. 9. The impact flux of $d > 10$ km leftover planetesimals the Moon (black line), Earth (blue), Venus (green), and Mars (red). The plot shows the accumulated number of impacts *since* time t (i.e., on the surface with age T), where $t = 0$ ($T = 4.57$ Ga) is the birth of the solar system, and $t \simeq 4.57$ Gyr ($T = 0$) is the present time. The profiles were normalized to having 4×10^5 $d > 10$ km planetesimals at $t = 42$ Myr, and $r_{out} = 1.5$ au. The vertical dash-dotted lines show $t = 42$ Myr and $t = 650$ Myr for reference. (For interpretation of the references to color in this figure legend, the reader is referred to the web version of this article.)

calibration to extrapolate the initial population from $r > 2$ au to 1.75–2 au (Section 4.1; Bottke et al., 2012; Nesvorný et al., 2017a). Here we considered different density profiles for $r < 1.75$ au. Specifically, employing the weighting scheme described in Section 4.3, we explored the effects of the planetesimal disk truncation at some outer radius, r_{out}. We tested $r_{out} = 1$, 1.25, 1.5 and 1.75 au. As for the effects of collisional grinding, the (intrinsic) collisional probabilities were found to be higher for disks truncated at smaller outer radii (the intrinsic collisional probability scales as $r^{5/2}$). The planetesimal population was dynamically removed faster, however, when the disk was truncated at smaller radii. These two effects pull in the opposite directions, and partially compensate each other.

As for the impact profiles, the cases with $r_{out} = 1.25$ au and 1.75 au produced results that were very similar to those obtained for $r_{out} = 1.5$ au. The profiles can be approximated by Eq. (4) with $\tau = 11.5$ Myr, assuming $\alpha = 0.5$, which is only a slightly shorter e-fold than $\tau = 12.2$ Myr inferred from the raw profiles. When α was allowed to adjust as well, however, a slightly better fit was obtained with $F = 3.8 \times 10^5$, $\tau = 6$ Myr and $\alpha = 0.45$ ($d > 10$ km and Earth). This is the parameterization of planetesimal impacts that we adopt in this work (Fig. 9). Note that having $\tau = 6$ Myr does not mean that the decline was faster than in the case with $\tau = 12.2$ Myr and $\alpha = 0.5$, because α is

now smaller (i.e., the exponential is more stretched). The half-life[13] of impact flux decline steadily increases with time; it is $t_{half} = 46$ Myr for $t = 200$ Myr and $t = 88$ Myr for $t = 650$ Myr. The case with $r_{out} = 1$ au could be interesting as well, but the planetesimal population declined more steeply in this case, and there are not as many late impacts as for $r_{out} = 1.25$–1.75 au.

The impact flux of leftover planetesimals on Venus closely follows the one obtained here for the Earth, but the overall impact rate is 1.4 times higher (for $r_{out} = 1.5$ au). The lunar impact flux is $\simeq 20$ times lower. The impact profile for Mars is flatter and can adequately be fit with $F = 8.2 \times 10^4$ for $d > 10$ km, $\tau = 6$ Myr and $\alpha = 0.42$ (Fig. 9). This means that the lunar chronology should not strictly be applied to Mars. For example, the Imbrium-age Mars ($t \simeq 650$ Myr or $T \simeq 3.92$ Ga) would have accumulated $\simeq 18$ times more planetesimal impacts than the same-age Moon, but a $t = 42$-Myr old Mars would have accumulated only $\simeq 4.1$ times more planetesimal impacts than the Moon (values given here for the whole target surfaces, not per km²). The Mars-to-Moon impact ratio is expected to change for $t > 1$ Gyr, when the asteroid impacts start to dominate (the ratio $\simeq 7$ is expected for asteroids; Section 4.1). The mean impact speeds of leftover planetesimals are 29.0, 23.2, 19.9 and 14.2 km s⁻¹ for Venus, Earth, the Moon, and Mars, respectively.

8. Lunar basins

We now turn our attention to lunar impacts. Fig. 10 shows the integrated history of lunar impacts including all major sources of impactors in the inner solar system: leftover planetesimals (Section 7), asteroids (Section 4.1), and comets (Section 4.2). We find that planetesimals dominated the early impact flux ($t < 1.1$ Gyr or $T > 3.5$ Ga; Morbidelli et al., 2018). Asteroids took over and produced most impacts in the last $\simeq 3.5$ Gyr. The cometary flux was never large enough, in the whole history of the inner solar system, to be competitive (the early instability at $t \lesssim 10$ Myr is adopted here).[14] In the first $\simeq 200$ Myr, comets produced more lunar impacts than asteroids, but the number of planetesimal impacts was far greater. Comets outpaced leftover planetesimals in the last ~ 3 Gyr, but that was when the overall impact flux was ruled by asteroids. This would suggest that isotopic and other signatures of comets may be difficult to find on the lunar surface.

The overwhelming majority of impacts observed on the lunar surface must date back to $T > 3.5$ Ga, when the impact flux was orders of magnitude higher than it is today. The model predicts $\simeq 500$ $d > 20$ km lunar impacts for $t > 42$ Myr ($T < 4.53$ Ga). For comparison, modeling the lunar gravity anomalies detected by GRAIL, Miljković et al. (2016) found $\simeq 50$ impacts of $d > 20$ km bodies (Section 2). We therefore see that the number of impacts suggested by our model would be excessive, by a factor of ~ 10, if the Moon surface recorded all large impacts since its formation (Zhu et al., 2019a).[15]

The Moon was fully molten when it accreted from the debris disk created by the giant impact on proto-Earth (see Canup et al., 2021, for a review). The subsequent evolution and solidification of the global lunar magma ocean (LMO) was controlled by a number of geophysical processes, including tidal heating, formation of an insulating flotation crust, etc. (Meyer et al., 2010; Elkins-Tanton et al., 2011). Radiogenic lunar crustal ages span from 4.47 to 4.31 Ga and suggest a prolonged stage of complete LMO solidification (Shearer, 2006; Elkins-Tanton et al., 2011; Maurice et al., 2020). The lunar basins that formed while the LMO was still present would have been subject to

---

[13] The number of impacts in a short interval Δt around t can be obtained as $dF/dt \times \Delta t$. The half-life of impact decline is $\delta t_{half} = \tau (t/\tau)^{1-\alpha}/(2\alpha)$.

[14] Comets could represent a more significant contribution to the lunar basin record only if the instability happened late. For example, to produce more than five lunar basins (i.e., $\gtrsim 10\%$ of all known basins), the instability would have to happen at $t \gtrsim 170$ Myr.

[15] It is possible that some younger basins erased older basins but it is difficult to imagine how this could account for the above quoted factor of ~ 10.
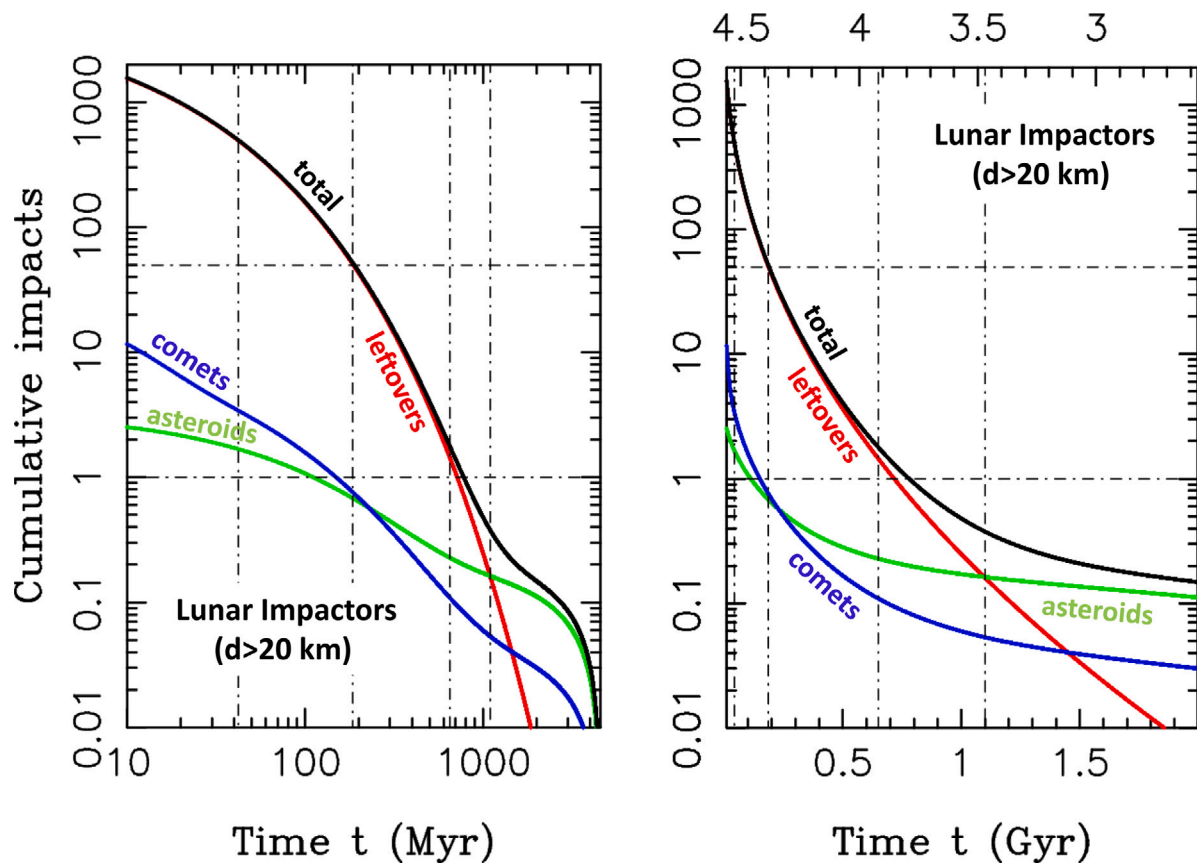
Fig. 10. Impacts of $d > 20$ km bodies on the Moon (log time scale in the left panel, linear on the right). The plot shows the accumulated number of impacts *since* time t, where $t = 0$ is the birth of the solar system, and $t \simeq 4.57$ Gyr is the present time. The planetesimal, asteroid and comet profiles are shows by red, green and blue lines, respectively; the black line is the total impact flux. The vertical dash-dotted lines show the Moon formation in our model ($t = 42$ Myr), estimated start of the known lunar basin record ($t \simeq 190$ or $T \simeq 4.38$ Ga), Imbrium formation ($t \simeq 650$ Myr or $T \simeq 3.92$ Ga), and transition from the planetesimal-dominated to asteroid-dominated impact stages ($t \simeq 1.1$ Gyr or $T \simeq 3.5$ Ga). The numbers on the upper axis of the left panel indicate time T (in Gyr) measured looking back from today. (For interpretation of the references to color in this figure legend, the reader is referred to the web version of this article.)

extreme relaxation that would have reduced topographic and crustal thickness signatures (Miljković et al., 2021). These early basins may be unidentifiable today.

The long-lived LMO would resolve the problem with the excess of planetesimal impacts on the young Moon. Suppose, for example, that the lunar surface started recording basin-scale impacts at $t \simeq 190$ Myr ($T \simeq 4.38$ Ga), or roughly 150 Myr after Moon's formation in our model — the oldest known basins (e.g., South Pole–Aitken) would date back to this time. If so, we would expect $\simeq 50$ $d > 20$ km impacts to be recorded (Fig. 10), in a close agreement with the lunar basin record. Concerning the LMO lifespan, Morbidelli et al. (2018) and Zhu et al. (2019a) reached similar conclusions — they proposed $T \simeq 4.35$ Ga — based on the HSE constraint (Section 14). Scaling to smaller impactor sizes, we estimate ~ 180 $d > 10$ km impacts for $T < 4.38$ Ga, in a close agreement with ~ 200 $D > 150$ km lunar craters inferred in Bottke and Norman (2017) (a $d = 10$ km impactor is assumed here to produce a $D = 150$ km lunar crater; Johnson et al., 2016a).

The time of LMO solidification, t_{LMO}, inferred here from the lunar basin record is uncertain. For example, for a slightly higher calibration with 5.2×10^5 $d > 10$ km planetesimals at $t = 42$ Myr, we obtain $t_{LMO} = 215$ Myr ($T_{LMO} \simeq 4.35$ Ga). If, instead, there only were 2.6×10^5 $d > 10$ km planetesimals at $t = 42$ Myr, then $t_{LMO} = 160$ Myr ($T_{LMO} \simeq 4.41$ Ga). Turning this argument around, the $T = 4.31$ Gyr age for the youngest known crustal ages would imply $t_{LMO} = 260$ Myr. This could suggest that our nominal calibration of leftovers is a factor of ~ 2 too low, and that there were $\sim 8 \times 10^5$ $D > 10$ km planetesimals at $t = 42$ Myr. It could indicate that the effects of collisional grinding were not as severe as we assumed here (e.g., stronger Q_D^* required).

It has to be noted that the LMO solidification is defined here in a specific context: the melt layer has to be thin enough for the topographic and crustal thickness signatures of basins to survive and be identifiable today. Miljković et al. (2021) showed that impact basins experience extreme relaxation for melt layers as thin as ~ 10 km (the melt layer needs to be close to the surface, Miljković et al. considered the melt layer in depths 10–50 km below the surface). Here we therefore provisionally interpret T_{LMO} as the time when the melt layer became thinner than 10 km. The youngest radiogenic crustal ages can post-date our T_{LMO}, because they mark the time when the LMO solidification was brought to completion.

Oceanus Procellarum is the largest of the lunar maria, covering roughly 10% of the total lunar surface. It is uncertain whether Procellarum is or is not an impact-generated basin (e.g., Andrews-Hanna, 2016). Here we estimate the probability of an impact of Ceres-class planetesimal on the Moon. Adopting the scaled asteroid-like distribution from Fig. 7 (green line), there would be ~ 100 $d > 1000$ km planetesimals for $t = 42$ Myr, each having a 0.4% of probability to impact on the Moon (Section 6). We can therefore roughly estimate that one $d > 1000$ km impact on the Moon for $t > 42$ Myr is a $\sim 40\%$ probability event (i.e., it *can* happen). This is consistent with the results reported in Zhu et al. (2019b), who considered impactor diameters $\simeq 500$–1000 km and found similarly large probabilities.

9. Imbrium-era impacts

Having established that (nearly) all lunar basins formed from impacts of leftover planetesimals (only ~ 0.7 and ~ 0.8 $d > 20$ km lunar

impacts of asteroids and comets are expected to happen for $t > 190$ Myr, respectively), we now consider the Imbrium-era impacts. What are our constraints? Evidence suggests that Imbrium formed at $T \simeq 3.92$ Ga ($t \simeq 650$ Myr; Zhang et al., 2019) by an impact of a $d \gtrsim 100$ km object (Miljković et al., 2013, 2016; Schultz and Crawford, 2016). From the crater counts we know that the Orientale and Schrödinger basins formed after Imbrium (e.g., Orgel et al., 2018). These smaller basins were produced by $d \simeq 50$–64 km and $d \simeq 20$ km impactors, respectively (Miljković et al., 2016; Johnson et al., 2016b).

Having only two smaller basins with post-Imbrium formation ages is surprising. Adopting the asteroid belt size distribution, we find that there should be ~ 7.4 $d > 20$ km impacts for every $d > 100$ km impact. The expected number of $d > 20$ km impacts would be even larger if we assumed a steeper size distribution (Minton et al., 2015). Our interpretation of this problem is that the Imbrium basin should have formed unusually late, by chance, relative to the expectation from the lunar impact chronology. In other words, statistically, the Imbrium basin formation needs to be an unusually late event.

The relatively late formation of some lunar basins is expected in our model. We find, for example, with the standard normalization considered here — 4×10^5 $d > 10$ km leftover planetesimals at $t = 42$ Myr, and the asteroid-like size distribution for $d > 10$ km — that on average $\simeq 2.3$ basins are expected to form for $t > 600$ Myr ($T < 3.97$ Ga; Fig. 10). Given the strong decline of planetesimal impacts for $t > 600$ Myr, any basin-scale impacts are expected to happen just after 600 Myr. As for Imbrium, we estimate that there should be $\simeq 0.31$ $d > 100$ km lunar impacts for $t > 600$ Myr, and that the Imbrium formation at $t > 600$ Myr should therefore be a $\simeq 23\%$ probability event (from the standard Poisson statistics), or 15%–35% considering the calibration uncertainty described in Section 5.

We now ask how likely it is for Imbrium to form late ($t > 600$ Myr, $d > 100$ km) *and* have exactly two basins (Orientale and Schrödinger, $d > 20$ km impactors) younger than Imbrium. This is a very restrictive conditions and the probability is therefore not expected to be high. But this is not the main point here. The main point is to understand whether a shorter or longer tail of impactors than the one obtained here, would fit data better. The condition is evaluated with our standard calibration of leftovers (see Nesvorný et al., 2022 for other calibrations). We fix $\alpha = 0.45$, vary τ in Eq. (4), and generate a statistically large number of random impact sequences in each case.

We find that the probability has a broad maximum around $\tau = 6$ Myr (Fig. 11), *which was the best-fit e-fold that we obtained for leftover planetesimals*. The probability drops for $\tau < 5$ Myr because it becomes very difficult to obtain any late impacts in this case. It decreases for $\tau > 6$ Myr, because too many basins form after Imbrium if the decline of the impact flux is too slow. It thus cannot be argued that a very slow decline of impactors would help to explain the lunar basin record. Instead, the impact chronology obtained here ($\alpha = 0.45$ and $\tau = 6$ Myr) is (nearly) optimal to satisfy the Imbrium-era constraints. A similar argument can be made about the overall normalization of leftover planetesimals. The results are not affected by small changes of the impact chronology. For example, the probability peaks at $\tau \simeq 9$–12 Myr when we use $\alpha = 0.5$ from Eq. (4), whereas $\tau = 12.2$ Myr was our best fit with $\alpha = 0.5$ (Fig. 8).

The Imbrium-era impactors are often found to be stored on orbits with $a \simeq 1.3$–1.7 au, $e < 0.2$, and in the mean motion resonances with Mars (e.g., 6:5, 7:6, 11:9; inside or outside of the Mars orbit). They either start with $a \simeq 1.3$–1.7 au at $t = 0$ or are scattered to 1.3–1.7 au from $\lesssim 1$ au. The resonances provide a phase-protection mechanism against collisions with Mars. The orbits have low eccentricities such that they do not cross the orbit of Earth. The bodies stay in the resonances for hundreds of Myr, are eventually released to orbits with higher eccentricities, at which point they can impact. This is an example of the "storage places" hypothesized by Wetherill (1975). We are only able to see this because our model self-consistently
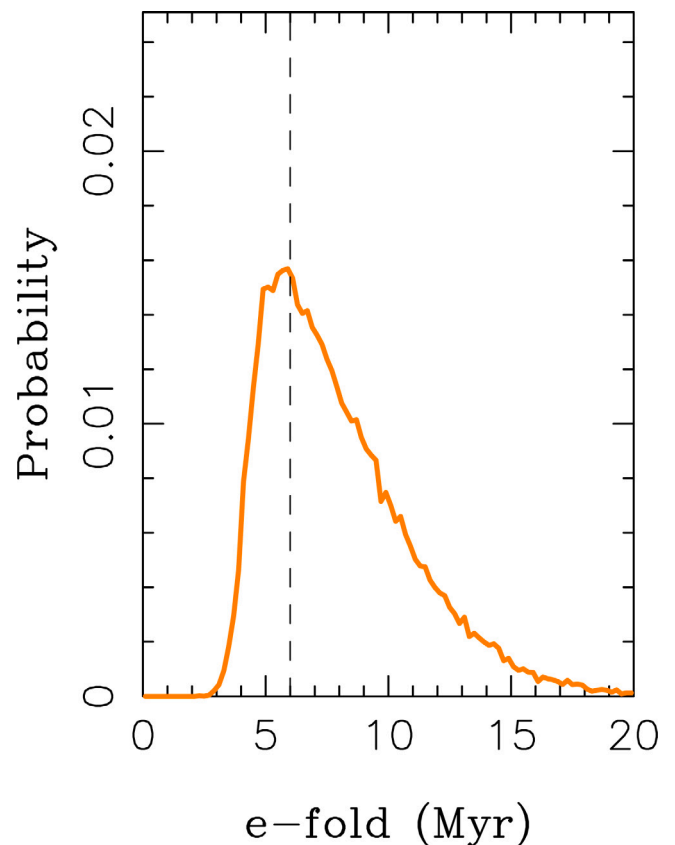

Fig. 11. The probability of matching the Imbrium-era constraints described in the main text as a function of the impact flux decline e-fold τ ($\alpha = 0.45$ and the standard calibration of leftover planetesimals). The vertical dashed line marks $\tau = 6$ Myr obtained from our dynamical modeling. (For interpretation of the references to color in this figure legend, the reader is referred to the web version of this article.)

followed the growth of the terrestrial planets and impact profile of leftover planetesimals (Sections 2 and 4.3).[16]

10. Lunar N_{20} chronology

To compare our model results with lunar chronologies we need to compute the cratering flux for small impactors. We start discussing the N_{20} chronology (Fig. 12A), where we have more confidence in the model results (given that no wild extrapolations to very small sizes are needed). For the lunar impact speeds of leftover planetesimals and asteroids obtained here (~ 20 km s^{-1}; Sections 4.1 and 7), we assume that a $d = 1$ km projectile makes a $D = 20$ km lunar crater (see Morbidelli et al., 2018 for a discussion of the scaling laws). The overall mean impact velocity of planetesimals on the Moon is lower ($v_i \simeq 17$ km s^{-1}), but the mean value is mainly contributed by the very early impactors that have, in general, lower impact speeds (because they are on orbits with $a \sim 1$ au). The mean impact speeds of planetesimals for $t > 200$ Myr are higher ($v_i \simeq 20$ km s^{-1}), and more similar to asteroids ($v_i \simeq 21$ km s^{-1}; Section 4.1). This gives some justification to using the same projectile size for both types of impactors.

To compute $N_{20}(T)$ from our impact model, we assume that the size distribution of leftover planetesimals for $1 < d < 10$ km was similar to that of today's asteroid belt (Section 5). There are roughly 1.1×10^6

---

[16] If we would switch to the real orbits of planets at $t = 42$ Myr, or at any other time during the simulation, the resonant planetesimals would be prematurely released and this would (presumably) produce a shorter impact tail.
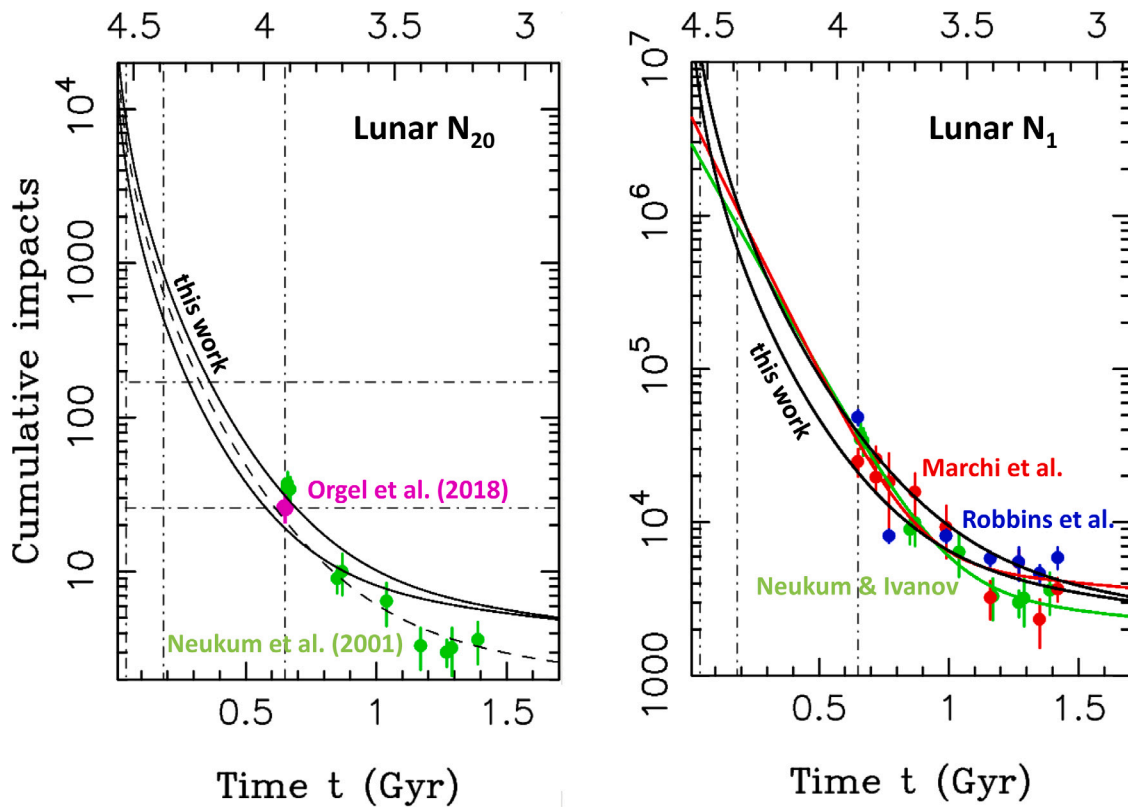
Fig. 12. Left: The lunar N_{20} chronology. The two black lines show our model chronologies with minimal (2.6×10^5 $d > 10$ km bodies at $t = 42$ Myr) and maximal (5.2×10^5 $d > 10$ km bodies at $t = 42$ Myr) calibrations of leftover planetesimals. The purple dot is the density of $D > 20$ km craters on Fra Mauro/Imbrium highlands (Fassett et al., 2012; Orgel et al., 2018). The green dots are the N_{20} values inferred for different terrains from Neukum et al. (2001). The dashed line shows a modified model chronology where the constant term of the asteroid flux was reduced by a factor of 2. Right: The lunar N_1 chronologies from this work (black lines), Neukum and Ivanov (1994) (green line and symbols), and Marchi et al. (2009) (red line and symbols). The crater counts from Robbins (2014) are shown by blue dots. The estimated uncertainties of different measurements are shown by vertical bars. The numbers on the upper axes indicate time T (in Gyr) measured looking back from today. (For interpretation of the references to color in this figure legend, the reader is referred to the web version of this article.)

main-belt asteroids with $d > 1$ km (Bottke et al., 2020) and $\simeq 8200$ with $d > 10$ km (Mainzer et al., 2019). We therefore scale the planetesimal flux profile from $d > 10$ km to $d > 1$ km by a factor $1.1 \times 10^6 / 8200 = 134$. This gives $F(1\,\text{km}) = 2.5 \times 10^6$ in Eq. (4) for the whole lunar surface ($\tau = 6$ Myr and $\alpha = 0.45$ from Section 7). The same scaling factor is used for the early flux of asteroids (the first term in Eq. (2)). The constant term in Eq. (2) for $d > 1$ km is obtained from $d > 1$ km NEAs at the present epoch. Morbidelli et al. (2020) estimated that the average time interval between $d > 1$ km NEA impacts on Earth is $\simeq 0.75$ Myr (also see Harris and D'Abramo, 2015). We thus have $F_2(1\,\text{km}) \simeq 1.3$ Myr^{-1} in Eq. (2).

Neglecting comets, which should only contribute at the $< 10\%$ level, a simple $N_{20}(T)$ chronology function — the number of accumulated $D > 20$ km craters in area 10^6 km^2 of the lunar surface since T — is given by

$$N_{20}(T) = a \exp[-(t/6\ \text{Myr})^{0.45}] + b \exp[-(t/65\ \text{Myr})^{0.6}] + cT \quad (5)$$

with $t = 4570 - T$ (t and T given in Myr), $a = 6.7 \times 10^4$, $b = 40$ and $c = 1.7 \times 10^{-3}$ Myr^{-1}. The first term in Eq. (5) stands for leftover planetesimals, the second and third for asteroids. The second term is much less important than the other two and can be discarded for a rough estimate of N_{20}. Fig. 12A compares our model chronology with crater densities measured for different lunar terrains.

Fassett et al. (2012) reported $N_{20} = 30 \pm 5$ for the $\simeq 3.92$ Gyr old Fra Mauro/Imbrium highlands. This value was slightly revised in Orgel et al. (2018), giving $N_{20} = 26 \pm 5$ (purple symbol in Fig. 12A), which nearly perfectly aligns with our model chronology obtained for the standard calibration of terrestrial planetesimals. We cannot plot $N_{20}(T)$ for other basins from Fassett et al. (2012) and Orgel et al. (2018)

in Fig. 12A, because their radiometric age is unavailable or uncertain. For reference, we also show data inferred from Neukum et al. (2001). For that, we take the N_1 values reported in Neukum et al. (2001) and scale them to N_{20} with the Neukum's "old" production function ($N_1/N_{20} \simeq 1000$). We believe this is a reasonable approach because the crater counts on old surfaces were typically done for relatively large craters, and were extrapolated down to N_1 with the same production function. Reporting them as N_{20} should therefore be equally valid.

The N_{20} value inferred from Neukum et al. (2001) for the Fra Mauro/Imbrium highlands is slightly larger than the more recent crater counts discussed above; it plots near the upper limit of our leftover calibration range. The results for young lunar maria are more discrepant. Here the N_{20} values inferred from Neukum et al. (2001) plot below our chronology function, indicating lower crater densities, and the difference becomes larger for younger lunar maria (Oceanum Procellarum, Mare Imbrium, Mare Crisium, Mare Fecundatis) than for the older ones (Taurus Littrow, Mare Tranquillitatis).

This may mean one of several things. At the face value, inferred N_{20} densities could indicate that our chronology function should more steeply drop for $T < 3.5$ Ga (the dashed line in Fig. 12A shows an example with $c = 0.85 \times 10^{-3}$ Myr^{-1}). For that to work, however, the Earth impact rate of $d > 1$ km asteroids at $T \simeq 3.1$–3.5 Ga would have to be lower, by a factor of ~ 2, than the current impact rate (e.g., Morbidelli et al., 2020; the current impact rate of large NEAs is known to a better than $\sim 10\%$ precision), suggesting the number of impacts would have to increase at some point in the last 3 Gyr (Culler et al., 2000; Mazrouei et al., 2019).

Another possibility is that the N_{20} values inferred from Neukum et al. (2001) for $T \simeq 3.1$–3.5 Ga are systematically a factor of ~ 2

lower. Note that the density of $d > 20$ km craters on young lunar maria is very low and subject to small number statistics. We therefore extrapolated from smaller craters, which were actually counted with some confidence, to estimate N_{20}. But perhaps the actual production function is flatter for $D \gtrsim 5$ km than the one we adopted from Neukum et al. (2001), and would thus give a larger N_{20} value.[17] Alternatively, the crater counts reported in Neukum et al. (2001) for young lunar maria may be lower than the actual values. The results of Robbins (2014) give some credit to this possibility, because their N_1 counts for young lunar maria (the *actual* counts of $D > 1$ km craters) are a factor of ~ 1.5–2 higher than N_1 from Neukum et al. (2001). If this difference propagates to N_{20}, it could be fully responsible for the problem shown in Fig. 12A.

Our chronology can be used to estimate the formation ages of lunar basins from N_{20} counts. For example, the age of the Nectaris basin with $N_{20} = 170$ per 10^6 km^2 (Orgel et al., 2018), is estimated to be $T = 4.21$–4.29 Gyr, where the uncertainty is dominated by the uncertain calibration of the lunar chronology function in Eq. (5) (here given for the two chronologies shown by solid lines in Fig. 12A). For comparison, Orgel et al. (2018) suggested a younger, $T = 4.17$-Gyr age for the Nectaris basin from the "old" Neukum chronology function.

11. Lunar N_1 chronology

We have less confidence in extrapolating our model results to $N_1(T)$, because very small bodies are subject to a host of dynamical (e.g., radiation effects; Vokrouhlický et al., 2015) and physical (e.g., rotational spin-up and mass loss) effects that were not modeled in this work. The small body populations such as the main asteroid belt are also not well characterized for $d < 1$ km. Some useful information can nevertheless be obtained by assuming that the impact flux of small asteroids was roughly constant in the last ~ 3 Gyr and equal to the impact flux of modern NEAs.

From the scaling laws we estimate that a $d \simeq 40$ m asteroid impactor would produce a $D \simeq 1$ km lunar crater.[18] There are $\sim 5 \times 10^5$ $d > 40$ m NEAs (Bottke et al., 2020; debiased data from updates of Harris and D'Abramo, 2015). Assuming the usual impact probability $p_i = 1.5 \times 10^{-3}$ Myr^{-1} of NEAs with the Earth (e.g., Morbidelli et al., 2020), and scaling things to the Moon, we obtain $c = 1.0$ Myr^{-1} (per 10^6 km^2 of lunar surface).[19] This estimate is consistent with a recent analysis of planetary impacts from small NEAs (Nesvorný et al., 0000).

There are no useful constraints on the population of $d > 40$ m leftover planetesimals. To obtain a rough estimate of $N_1(T)$ for $T > 3.5$ Ga, we adopt $N_1/N_{20} = 1400$ from Morbidelli et al. (2018) (also see Marchi et al., 2012). Note that this is just a reference ratio that turns out to give an acceptable fit to the N_1 data (Fig. 12B). This does not mean, however, that the adopted value is strictly correct. For example, a somewhat higher calibration of leftover planetesimals (e.g., 5.2×10^5 $d > 10$ km planetesimals at $t = 42$ Myr) would still fit the data in

Fig. 12A) quite well. If that calibration is adopted, $N_1/N_{20} \sim 1000$ — consistent with the "old" production function from Neukum et al. (2001) — would work well in Fig. 12B.

Neglecting comets, a simple $N_1(T)$ chronology function — the number of accumulated $D > 1$ km craters in the area 10^6 km^2 of lunar surface since T — is given by

$$N_1(T) = a \exp[-(t/6 \text{ Myr})^{0.45}] + b \exp[-(t/65 \text{ Myr})^{0.6}] + cT \quad (6)$$

with $t = 4570 - T$ (t and T in Myr), $a = 9.4 \times 10^7$, $b = 5.6 \times 10^4$ and $c = 1.0$ Myr^{-1} (again, the second term is much less important than the other two and can be neglected). The c coefficient is only $\simeq 16\%$ higher than the one in Eq. (1) (Neukum et al., 2001; the one Eq. (1) needs to be multiplied by 10^3 to have the number of craters per Myr per 10^6 km^2, which are the units used here). The main difference with respect to Eq. (1) in Neukum et al. (2001) is that the first term in Eq. (1) is an exact exponential function, whereas here we have a stretched exponential in Eq. (6).

Fig. 12B compares our $N_1(T)$ chronology, with all the caveats mentioned above, to various crater counts and chronologies from Neukum et al. (2001) and Marchi et al. (2009). The main focus in Fig. 12B is the data from Robbins (2014) (blue dots in Fig. 12B), which are the *actual* counts of $D \sim 1$ km craters for Apollo and Luna landing sites; all other "data" points are the extrapolations from counts of larger craters.[20]

The N_1 crater counts from Robbins (2014) are slightly higher, in general, that the extrapolations from Neukum et al. (2001) and Marchi et al. (2009) (except for the old Mare Tranquillitatis age). They plot near the higher end of our chronology range (i.e., near the higher end of planetesimal calibration), but the agreement is reasonably good. While this gives some justification to the choice of parameters described above, we caution that other choices would potentially work as well. In particular, there is a degeneracy between the leftover planetesimal calibration and the N_1/N_{20} factor. If, for example, the NEA population were taken as a guide, and assuming that $d = 40$ m ($d = 1$ km) impactors make $D = 1$ km ($D = 20$ km) craters, we would find $N_1/N_{20} \sim 540$, a factor of 2.6 below the N_1/N_{20} value adopted above. To obtain $N_1/N_{20} \sim 1400$ from the NEA population, one would have to assume that a $d = 25$–30 m impactor makes $D = 1$ km lunar crater.

Comparing N_{20} from Fassett et al. (2012) with N_1 from Neukum et al. (2001), both for Fra Mauro/Imbrium highlands, gives $N_1/N_{20} \simeq 1400$. With N_1 for Fra Mauro/Imbrium highlands from Robbins (2014), we get $N_1/N_{20} \simeq 1800$. Playing the same game for the young lunar maria, where the N_1 counts are secure (Robbins, 2014), but the N_{20} counts require an extrapolation (Neukum et al., 2001), gives $N_1/N_{20} \sim 700$. Overall, these values may indicate that there was a trend of N_1/N_{20} with T, with the younger terrains showing lower N_1/N_{20} values than the old terrains. If this is interpreted in terms of the crater scaling laws, it would hint on a time dependence of the impactor-to-crater ratio (e.g., related to the depth of porous megaregolith; Le Feuvre and Wieczorek, 2011). If this is interpreted in terms of the size distribution of impactors, we would speculatively infer that the size distribution of leftover planetesimals below $d \simeq 1$ km was (slightly) steeper than that of modern NEAs.

Additional N_1 calibration data point comes from the analysis of Chang'e-5 samples by Che et al. (2021), who found $N_1(T) = 1200$–1800 (per 10^6 km^2) for a $T = 1963 \pm 57$ Ma old lunar terrain. Using the standard $N_1(T)$ chronology from Eq. (6), we find $N_1(T) \simeq 1980$ for $T = 1963$ Ma — only a slightly higher value than N_1 reported by Che et al. (2021). This is consistent with the observation made in Che et al. (2021) that the existing chronology curves, which are calibrated on very young lunar terrains ($T < 1$ Ga; Cone, Tycho, North and South Ray craters; Neukum et al., 2001; Marchi et al., 2009; Hiesinger et al., 2012), fall above the N_1 value obtained from Chang'e-5 samples. This may indicate that the impact flux at $T \simeq 2$ Ga may have been slightly lower (by $\simeq 20\%$) than the one estimated here.

---

[17] Scaling N_1 from Neukum et al. (2001) to N_{20} with the "new" production from Neukum and Ivanov (1994) ($N_1/N_{20} \simeq 420$) would resolve the problem with the young lunar maria in Fig. 12A, but this would move Imbrium's N_{20} to a factor of $\simeq 3$ above N_{20} from Fassett et al. (2012) and Orgel et al. (2018). Thus, in some sense, N_1/N_{20} needs to be higher for Imbrium and lower for young lunar maria.

[18] The impactor size adopted here is intermediate between the one used in Morbidelli et al. (2018), $d = 50$ m, and Marchi et al. (2021), $d = 33$ m — see the discussion of scaling laws in these papers.

[19] This calibration works well to reproduce the crater counts on very young lunar terrains ($T < 1$ Ga; Cone, Tycho, North and South Ray craters; Neukum et al., 2001; Marchi et al., 2009; Hiesinger et al., 2016), when the standard production functions are used to extrapolate the counts from very small craters to N_1. We do not discuss the young terrains in detail here, because we believe that a NEA-derived N_1 value for $T < 1$ Ga is better constrained than the one obtained from counts of $D < 100$ m craters.

[20] We do not show the chronology function from Robbins (2014), but note that their data-driven fit has a very different shape.
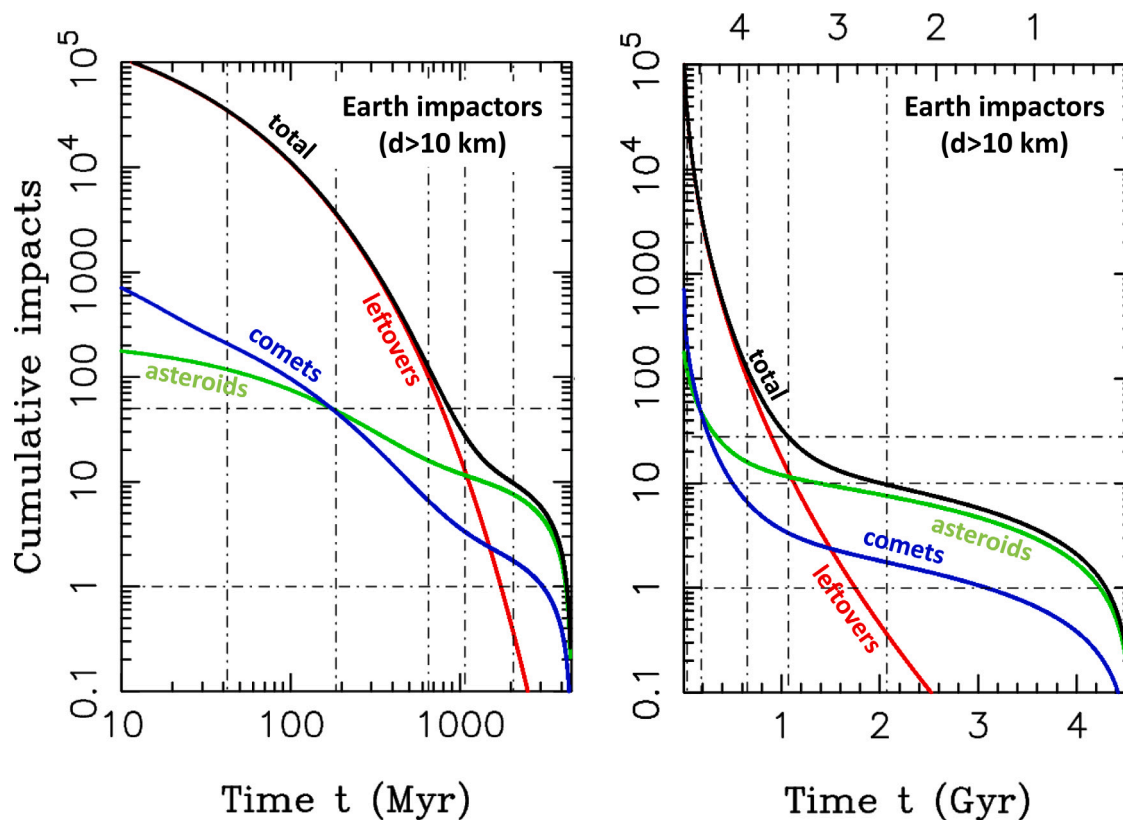
Fig. 13. Impacts of $d > 10$ km bodies on the Earth. The vertical dash-dotted lines show the Moon formation in our model ($t = 42$ Myr), estimated start of the known lunar basin record ($t \simeq 190$ or $T \simeq 4.38$ Ga), Imbrium formation ($t \simeq 650$ Myr or $T \simeq 3.92$ Ga), and the beginning/end of the late Archean period ($T = 2.5$–3.5 Ga). The numbers on the upper axis of the left panel indicate time T (in Gyr) measured looking back from today.

12. Archean spherule beds

When a large impactor strikes the Earth, it produces a vapor-rich ejecta plume containing numerous small melt droplets, most of which rise above the atmosphere. As the plume cools down, glassy spherules form and fall back, producing a global layer that can be several millimeters (for a Chicxulub-sized impact event) to many centimeters thick (Johnson and Melosh, 2012). The late Archean (2.5–3.5 Ga) spherule beds are thicker than those associated with the 66 million years old, 180 km wide Chicxulub crater — estimated $d \sim 10$ km impactor (Collins et al., 2020) — and should have therefore been produced by $d > 10$ km impactors (Bottke et al., 2012; Johnson et al., 2016a). Some ~ 16 spherule beds have been found in the late Archean (e.g., Marchi et al., 2021), although preservation biases and incomplete sampling may be an issue. At least some of these layers may have been produced by very large, $d \sim 50$ km impactors.

The impact flux of $d > 10$ km bodies on the Earth is shown in Fig. 13. We find $\simeq 20$ $d > 10$ km impacts on the Earth for $T = 2.5$–3.5 Ga. This is similar to the number of known spherule beds in the late Archean period.[21] The leftover planetesimals and main-belt asteroids contribute equally to impacts in this time frame (~ 10 impacts each).

---

[21] The known Archean spherule beds occur in two distinct time intervals, 2.4–2.7 Ga and 3.2–3.5 Ga (e.g., Lowe and Byerly, 1986; Byerly et al., 2002; Glass and Simonson, 2013; Lowe et al., 2014; Schulz et al., 2017; Ozdemir et al., 2019; see Marchi et al., 2021 for a recent review). If they are indicative of the average flux in the late Archean, there should be ~ 14 additional spherule beds at 2.7–3.2 Ga. If so, the number of $d > 10$ km impacts in our model would represent $\sim 60\%$ of the total number of spherule beds. For reference, some ~ 43 $d > 7$ km impacts on the Earth are expected in our model at 2.5–3.5 Ga (scaled from $d > 10$ km to $d > 7$ km with the size distribution of main belt asteroids).

Whereas the asteroid impacts were more uniformly spread over late Archean, nearly all planetesimal impacts should have happened for $T > 3$ Ga. The model predicts that ~ 10 and ~ 2.2 $d > 10$ km asteroids should have impacted the Earth in the last 2.5 and 0.6 Gyr, respectively. Assuming that the number ratio of $d > 10$ km to $d > 50$ km impactors is 8.9, as inferred from the size distribution of main belt asteroids, the model implies ~ 2 $d > 50$ km impactors in late Archean.

13. Martian crater chronology

The impact flux of $d > 20$ km impactors on Mars is shown in Fig. 14. The Martian impact profile is different from that of the Moon, Earth and Venus. The impact profile is more extended in time and has a longer tail of late impacts. This is simply because leftover planetesimals at ~ 1.5 au live longer and can impact later. The transition from the planetesimal-dominated to asteroid-dominated impact stages thus probably occurred later for Mars than for the Moon ($t \simeq 1.4$ Gyr vs. $t \simeq 1.1$ Gyr). The impact flux of leftover planetesimals on Mars is more sensitive to r_{out} than that of any other terrestrial world. The results shown in Fig. 14 were obtained for our nominal case with $r_{out} = 1.5$ au (and 4×10^5 $d > 10$ km planetesimals at $t = 42$ Myr). The overall number of planetesimal impacts on Mars is $\simeq 1.4$ times lower for $r_{out} = 1.25$ au, and $\simeq 2$ lower for $r_{out} = 1$ au. This would reduce the planetesimal contribution and shift the transition back in time.

Following the method described in Section 11, the $N_1(T)$ chronology (per 10^6 km²; Fig. 16) for Mars can be given as

$$N_1(T) = a \exp[-(t/6 \text{ Myr})^{0.42}] + cT \tag{7}$$

with $a = 3.7 \times 10^7$ and $c = 0.41$ Myr⁻¹. The second term in Eq. (6) — corresponding to the early impact flux of asteroids — in not included here for simplicity. Here we truncated the planetesimal disk at $r_{out} = 1.5$ au (at $t = 0$). The contribution of leftover planetesimals is $\simeq 2$
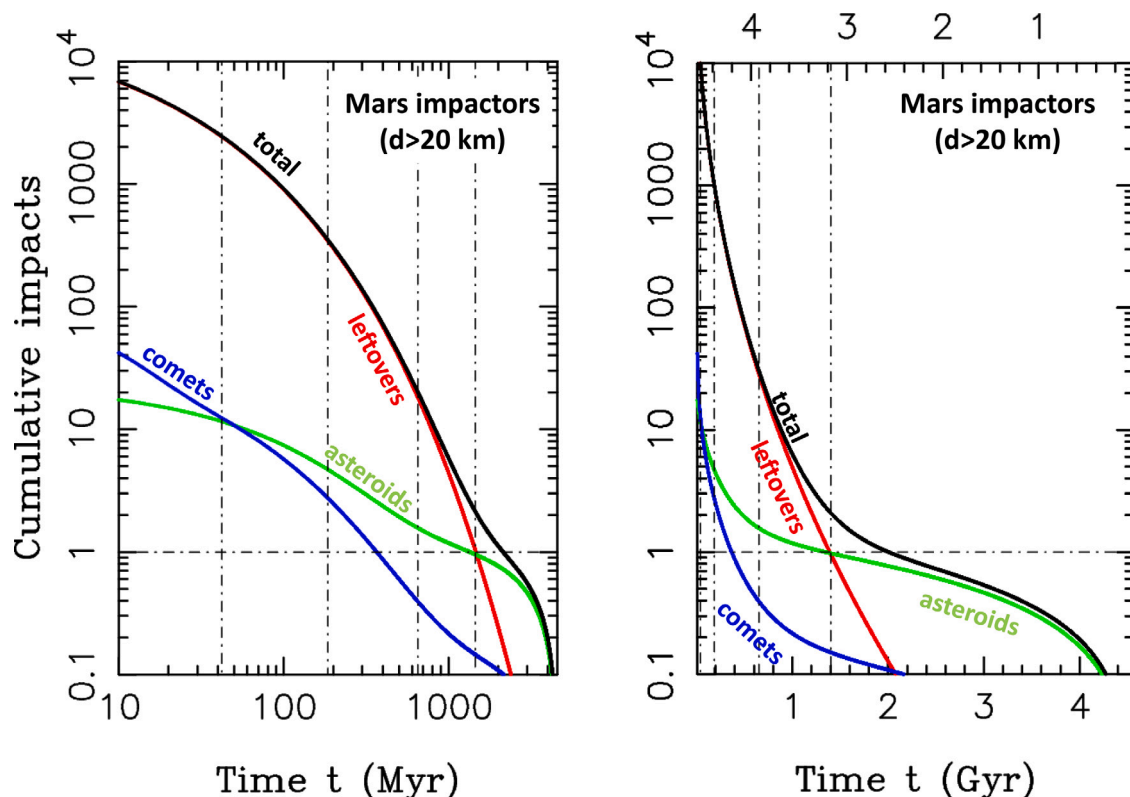
Fig. 14. Impacts of $d > 20$ km bodies on Mars. The plot shows the accumulated number of impacts *since* time t (i.e., on the surface with age T), where $t = 0$ ($T = 4.57$ Ga) is the birth of the solar system, and $t \simeq 4.57$ Gyr ($T = 0$) is the present time. The vertical dash-dotted lines show the Moon formation in our model ($t = 42$ Myr), estimated start of the known lunar basin record ($t \simeq 190$ or $T = 4.38$ Ga), Imbrium formation ($t \simeq 650$ Myr or $T = 3.92$ Ga), and transition from the planetesimal-dominated to asteroid-dominated impact stages for Mars ($t \simeq 1.4$ Gyr or $T = 3.2$ Ga). The profiles were normalized to having 4×10^5 $d > 10$ km planetesimals at $t = 42$ Myr, and $r_{out} = 1.5$ au. The numbers on the upper axis of the left panel indicate time T (in Gyr) measured looking back from today.

times lower for $r_{out} = 1$ au; hence $a = 1.9 \times 10^7$ for $r_{out} = 1$ au. The asteroid branch — factor c in Eq. (7) — is rescaled from lunar $c = 1.0$ Myr^{-1} (Eq. (6)) using input from the dynamical models of modern NEAs (e.g., Granvik et al., 2018). The models indicate $R_b \simeq 1.2$ for small NEAs (Nesvorný et al., 0000), where R_b is the number ratio of Mars-over-Moon impacts normalized to a unit surface area; Hartmann and Neukum, 2001). Note that this value is much lower than the one adopted in Hartmann (2005) and Marchi (2021), $R_b \simeq 2.6$.

We assume the impact velocities 14–15 km s^{-1} for Mars and 19–20 km s^{-1} for the Moon, fold in the effect of different surface gravities of the Moon and Mars, and estimate that Mars requires a ~ 1.4 times larger impactor than the Moon to create a $D = 1$ km crater (Johnson et al., 2016a). Our reference asteroid size distribution (Harris and D'Abramo, 2015; Bottke et al., 2020) has a steep slope for $20 < d < 50$ m with the cumulative power index $\simeq 3.2$. The Martian $N_1(T)$ in Eq. (7) is therefore penalized by a factor of $1.4^{3.2} \simeq 2.9$ relative to the lunar chronology. We use the same penalization for the planetesimal and asteroid branches.

Fig. 15 compares the Martian chronology obtained here with the chronologies from Hartmann (2005), Werner et al. (2014) and Marchi (2021). We plot two chronologies from Eq. (7), one for $r_{out} = 1$ au (thin black line) and $r_{out} = 1.5$ au (thick black line), to illustrate the dependence on the initial planetesimal profile. There is a significant difference between the two (the planetesimal branch of $N_1(T)$ is a factor of $\simeq 2$ lower for $r_{out} = 1$ au). This is bad news for the prospect of accurate dating: the age estimates derived from the two chronologies differ by up to ~ 200 Myr for $T > 2$ Gyr. But this can be good news for the prospect of constraining the radial extension of the planetesimal disk from the Martian crater record — assuming that the radiometric age of an old Martian terrain with known N_1 will be measured in the near future (e.g., NASA Mars 2020).

The asteroid branches ($T < 2.5$ Ga) of the Hartmann (2005) and Werner et al. (2014) chronologies are a factor of ~ 1.5 higher and lower, respectively, that the one derived here. We find a good agreement with the chronology of Marchi (2021) for $T < 2$ Ga.[22] Looking back in time, the Hartmann, Werner, and Marchi chronologies continue relatively flat to $T > 3$ Ga, where they show a sharp bend upward. Our chronologies instead connect to the planetesimal branch and start raising already at $T \sim 2.5$ Ga.

Our best age estimate for the Noachian/Hesperian and Hesperian/Amazonian boundaries is 3.4–3.6 Ga and 2.6–2.9 Ga (the range given here for $r_{out} = 1$–1.75 au and the standard calibration of leftover planetesimals). Here we adopt the crater densities $N_1 = 4.8 \times 10^3$ and $N_1 = 1.6 \times 10^3$, both per 10^6 km^2, as defining the two boundaries (Tanaka, 1986; Hartmann, 2005). The Jezero crater — relevant to the NASA Mars 2020 mission — is estimated to be 2.2–2.5 Gyr old for $N_1 = 1.1 \times 10^3$ per 10^6 km^2 from Warner et al. (2020) or 2.4–2.7 Gyr old for $N_1 = 1.5 \times 10^3$ per 10^6 km^2 from Shahrzad et al. (2019).

For illustrative purposes, following the traditional approach (e.g., Hartmann and Neukum, 2001; Hartmann, 2005; Werner et al., 2014; Marchi, 2021), we also approximately rescale our lunar chronology from Eq. (6) to Mars. For that, we use $R_b = 1$ (roughly applicable for $r_{out} = 1.25$–1.75 au) for the planetesimal branch and $R_b \simeq 1.2$ for the asteroid branch (Nesvorný et al., 0000), and penalize Martian $N_1(T)$ by the factor of 2.9 to account for the impact velocity and surface gravity difference. For comparison, Marchi (2021) used $R_b = 0.5$ for planetesimals from Morbidelli et al. (2018), which is smaller than

---

[22] This is somewhat a coincidence because Marchi (2021) adopted $R_b = 2.6$ for asteroids, a steeper size distribution for $d = 20$–50 m and an additional 0.81 reduction factor from Popova et al. (2003).
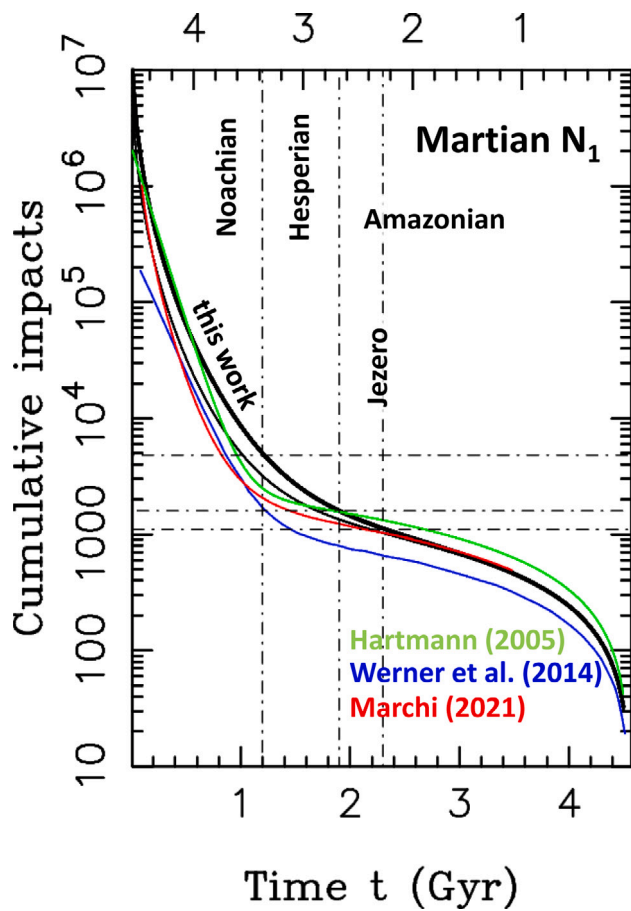
Fig. 15. The $N_1(T)$ chronologies for Mars. The bold and thin black lines show our Martian chronologies for $r_{out} = 1.5$ au and $r_{out} = 1$ au, respectively. For comparison, we also show the Martian chronologies from Hartmann (2005, green line), Werner et al. (2014, blue), and Marchi (2021, red); early instability/NEA scaling). The horizontal dot-dashed lines are the crater counts for Noachian/Hesperian and Hesperian/Amazonian boundaries, and for the Jezero crater terrains. The vertical dashed lines are our age estimates for these units in the model with $r_{out} = 1.5$ au. The ages inferred with $r_{out} = 1$ au are ~ 200 Myr older. The numbers on the upper axis indicate time T (in Gyr) measured looking back from today. (For interpretation of the references to color in this figure legend, the reader is referred to the web version of this article.)
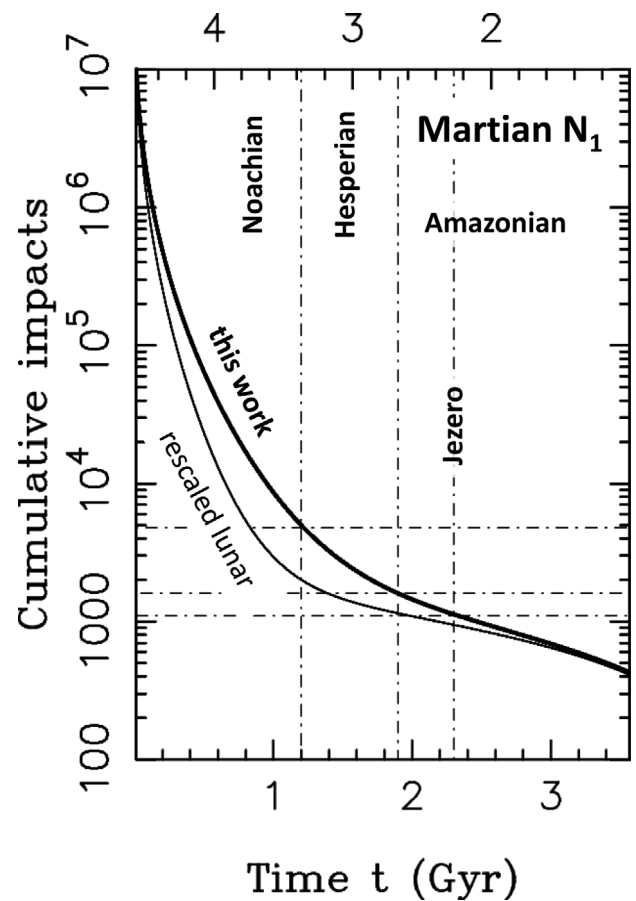
Fig. 16. A comparison of lunar and Martian chronologies. The thin solid line is the lunar $N_1(T)$ chronology rescaled to Mars as described in Section 13. The bold solid line is the Martian chronology inferred in this work for the standard calibration of leftover planetesimals and the original planetesimal disk truncated at 1.5 au (Eq. (7)). The horizontal dot-dashed lines are the crater counts for Noachian/Hesperian and Hesperian/Amazonian boundaries, and for the Jezero crater terrains. The vertical dashed lines are our age estimates for these units. The ages inferred from the rescaled lunar chronology would be ~ 400–500 Myr older. The numbers on the upper axis indicate time T (in Gyr) measured looking back from today.

our value, presumably because their terrestrial formation model was effectively run with $r_{out} \sim 1$ au. Indeed we find $R_b = 0.63$ for $r_{out} \sim 1$ au (statistics based on all impacts). This is consistent with a smaller planetesimal contribution for disks truncated at $r_{out} \sim 1$ au (for Mars, not in general — the planetesimal branch for the Earth is only slightly steeper for $r_{out} = 1$ au than for $r_{out} = 1.5$ au, and the overall number of terrestrial impacts remains nearly the same — again adopting 4×10^5 $d > 10$ km planetesimals at $t = 42$ Myr, independently of r_{out}). Fig. 16 shows that the Mars chronology function is more extended in time than the lunar chronology, implying that R_b is time dependent. *Applying the lunar chronology function to Mars can lead to inaccurate age estimates that can differ, by up to ~ 500 Myr, from the age estimates obtained from the accurate Martian chronology.*

Scaling from the most densely cratered surfaces of the Moon and Mars, Bottke and Norman (2017) estimated ~ 200 $D > 150$ km craters over the whole lunar surface, and ~ 500 $D > 150$ km craters over the whole Martian surface. From the scaling laws we find that a $d \simeq 10$ km impactor is needed to produce a $D = 150$ km crater on the Moon, and a $d \simeq 13$ km impactor is needed to make a $D = 150$ km crater on Mars (Holsapple and Housen, 2007; Johnson et al., 2016b; Morbidelli et al., 2018). In Section 8, we estimated ~ 180 $d > 10$ km lunar impacts for $T < 4.38$ Ga, which is consistent with Bottke and Norman (2017),

assuming that the lunar surface recorded $D > 150$ km craters since $T \simeq 4.38$ Ga (presumably the LMO solidification time). To obtain ~ 500 $D > 150$ km craters for Mars with our model-derived impact flux, we infer that the Martian surface would have to record $D > 150$ km craters since $T \simeq 4.27$ Ga for $r_{out} = 1.5$ au, and $T \simeq 4.35$ Ga for $r_{out} = 1$ au. Morbidelli et al. (2018) noted the same problem and suggested a global resurfacing event at $T \sim 4.4$ Ga, perhaps associated with the formation of the Borealis basin. There is currently no evidence for the late formation of Borealis. Robbins (2022) proposed that the formation of Borealis basin could have kept the surface warm enough for long enough to prevent large craters/basins from forming for an extended period of time. The volcanic and fluvial resurfacing of early Mars (Hartmann and Neukum, 2001) would have to be extremely powerful to globally erase $D > 150$ km craters for $T > 4.3$–4.4 Ga.

14. Discussion

We find that the terrestrial-zone planetesimals were the dominant source of lunar impactors for $T > 3.5$ Ga, and that asteroids were the dominant source of impactors for $T < 3.5$ Ga. This is in line with

the findings of Morbidelli et al. (2018).[23] The leftovers are expected to evolve collisionally (Bottke et al., 2007)[24] and reach an asteroid-belt-like size distribution in only ∼ 20 Myr after the first solar system solids. The size distribution of lunar impactors in the last 3.5 Gyr should be similar to that of modern NEAs. The modern NEAs evolve from the asteroid belt by size-dependent radiation processes which favor mobility of very small bodies (Vokrouhlický et al., 2015). They therefore have slightly steeper size distribution for $d < 10$ km than the main belt. This explains why the crater size distribution on ancient lunar craters is related to the main belt asteroids, and why the modern impactors have a NEA-like size distribution (Strom et al., 2005). Head et al. (2010) suggested that the transition between the two populations of impactors happened ∼ 3.5 Ga, which is what we find here from dynamical modeling.

Minton et al. (2015) pointed out that the asteroid-like size distribution of early lunar impactors would produce too many mega-basins ($D > 1200$ km) and suggested that the size distribution of impactors below $d \simeq 100$ km was somewhat steeper than that of today's asteroid belt. Johnson et al. (2016a) reiterated that point and proposed that the lunar basin data and Archean spherule beds could best be fit with a main-belt-like size distribution of impactors for $d \lesssim 50$ km, and a steeper slope for $d \gtrsim 50$ km. Here we find that the ancient impactors were leftover planetesimals from the terrestrial planet zone ($r \lesssim 1.5$ au), not asteroids. This makes it easier to understand any inferred differences. Note, however, that the size-distribution break at $d \sim 50$ km would imply fewer Imbrium impacts, and would diminish the probability of the late Imbrium formation in our model.

We showed that the lunar crater record is consistent with having $(2.6–5.2) \times 10^5$ $d > 10$ km planetesimals in the terrestrial planet zone (∼ 0.5–1.5 au) at ∼ 50 Myr after the first solar system solids. The collisional evolution in the first ∼ 20 Myr would have been stronger for higher initial planetesimal mass and weaker for lower initial mass. We therefore cannot predict, from the collisional modeling alone, the initial planetesimal mass. All that we can say is that there was at least ∼ 0.1 M_{Earth} in planetesimals to start with. This is significant, however, because it shows that there *was* a large population of planetesimals to start with. The formation models where the terrestrial planets grow from cm-size pebbles (e.g., Johansen et al., 2021) do not postulate any large planetesimal population in the terrestrial planet zone (they do not exclude it either).

Using the lunar basin record as a constraint on the LMO solidification (Section 8), we found that the LMO should have lasted to $T = 4.36–4.42$ Ga, roughly 160–210 Myr after the first solar system solids, and ∼ 110–160 Myr after the Moon-forming impact in our model (Section 2). Morbidelli et al. (2018) reached similar conclusions based on considerations related to the HSEs in the lunar mantle. They considered the possibility that HSEs were sequestered from the mantle of the Earth during magma ocean crystallization, due to iron sulfide exsolution (Rubie et al., 2016), and showed that this likely affected the Moon as a well (if the lunar mantle overturn is taken into account; Elkins-Tanton et al., 2011). The HSE would accumulate in the lunar mantle only after the LMO crystallization, estimated to happen ∼ 100–150 Myr after the Moon formation. This would correspond to ∼ 150–200 Myr after the solar system solids if the Moon formed at $t \sim 50$ Myr.

Fig. 17A shows the HSE constraints for the Earth, Mars, and Moon. Assuming chondritic composition of impactors it has been inferred that these worlds accreted 3×10^{25} g, 1.6×10^{24} g, and 1.5×10^{22} g during the Late Veneer (i.e., aftertheir differentiation is fully over such that

the accreted HSEs do not sink to the core). Assuming 30% retention of impactor mass for the Moon (Zhu et al., 2019a), we find that the LMO would have to solidify at $t \sim 200$ Myr ($T \sim 4.37$ Ga) to explain lunar HSEs. This is in an excellent agreement with the results of Morbidelli et al. (2018). The Earth differentiation should have ended within ∼ 10 Myr after the Moon-forming impact (e.g., Elkins-Tanton et al., 2011). We find that the accreted mass for $t > 50$ Myr is a factor of ∼ 3 too low to explain Earth's HSEs (it would be a factor of ∼ 10 too low if the Moon-forming impact happened at $t \sim 120$ Myr; Maurice et al., 2020; Kruijer et al., 2021). This shows the need for the accretion of very large planetesimals (∼ 1000–3000 km; Bottke et al., 2010; Marchi et al., 2014). The contribution of very large planetesimals to Earth's HSEs was not accounted for in Fig. 17A, because we adopted a steep size distribution for $d > 100$ km (Fig. 7). The stochastic accretion of very large planetesimals could help to explain the large difference in the HSE content between the Moon and Earth (∼ 2000; Bottke et al., 2010).[25]

If Mars accreted and differentiated early ($t \lesssim 10$ Myr, Dauphas and Pourmand, 2011; Marchi et al., 2020), it would have accreted ∼ 5×10^{25} g in our model during the Late Veneer (in small planetesimals). This is a factor of ∼ 3 higher than the late addition of chondritic material inferred from Martian meteorites (shergottite-nakhlite-chassigny, SNC; Marchi et al., 2020). It is possible that the average mantle abundance of HSEs is underestimated, perhaps because the average mantle abundance may be difficult to establish from (heterogeneous) SNC meteorites, or perhaps because our SNC collection is not fully representative of the Martian mantle. The retention of impactor mass could contribute as well. In Fig. 17A, we assumed a 100% retention factor for Mars but at least some work indicates that the retention factor may be lower (e.g., ∼ 60% in Artemieva and Ivanov, 2004). Finally, as we already discussed, the impact flux of planetesimals on Mars is lower when the disk of terrestrial planetesimals is truncated at the lower orbital radius. For example, if $r_{\mathrm{out}} \simeq 1$ au, instead of $r_{\mathrm{out}} = 1.5$ au that we used in Fig. 17A, the accreted mass would be reduced by a factor of $\simeq 2$.

The cometary impact profile is more extended in time than previously thought (Morbidelli et al., 2018). This is a consequence of the much improved statistic of simulations reported in Section 4.2. With the standard comet calibration, accounting for spontaneous comet disruptions, and assuming that the Moon-forming impact happened ∼ 50 Myr ($T \sim 4.52$ Ga) after the birth of the solar system, we find that the Earth would have accreted ∼ 1.5×10^{22} g of cometary material for $T < 4.52$ Ga (Fig. 17B). This is consistent with comets being the source of noble gasses in the Earth atmosphere (Marty et al., 2016). The mass accreted in cometary material would be larger if: (i) some comets fade instead of disrupting (Fig. 17B), (ii) the instability happened later, or (iii) the Moon formed earlier. In fact, the noble gas argument can be used to roughly constrain the delay between the instability and Moon formation, Δt. From Fig. 17B we infer $20 < \Delta t < 60$ Myr, with the exact value depending on the physical lifetime of comets (Section 4.2). This suggests, if the instability happened very early ($t < 10$ Myr; Clement et al., 2018; Liu et al., 2022), that the Moon must have formed early as well ($t < 70$ Myr or $T > 4.5$ Gyr; Thiemens et al., 2019).

We reported the impact profiles of leftover planetesimals from the best terrestrial planet formation simulation from Nesvorný et al. (2021a). This falls short, given that only one case was tested, to understand the possible variability of the impact profiles when different assumptions are made. This should be the focus of future investigations. If the variability is large, it would perhaps be possible to rule out/confirm some specific setups based on the lunar crater constraints.

---

[23] Brasser et al. (2020), instead, suggested that the early impact record was dominated by bodies from the E-belt.

[24] Unlike Bottke et al. (2007), we find that the effects of collisional grinding were not strong enough to prevent the leftover planetesimals from producing the dominant share of lunar basins.

[25] A great share of this difference is explained by the smaller accretional cross-section of the Moon (factor of ∼ 20, focusing included), long-lived lunar LMO (factor of ∼ 10), and lower retention factor of the Moon (factor of ∼ 3; Zhu et al., 2019a).
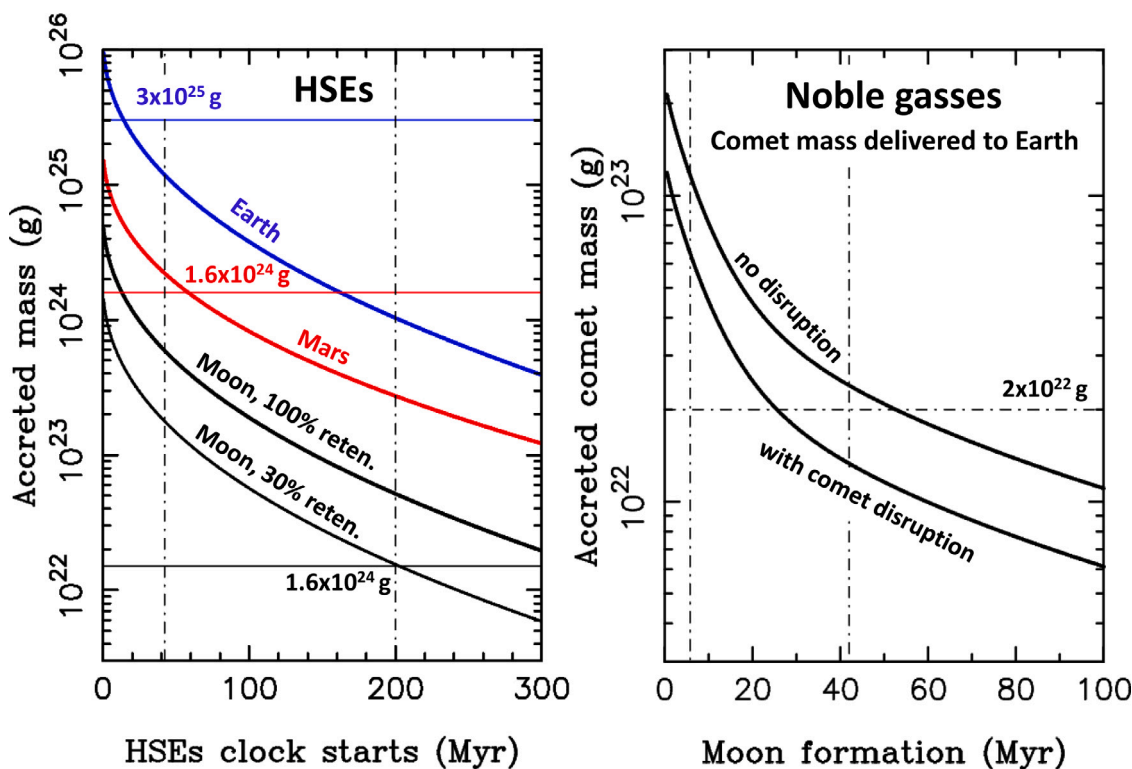
Fig. 17. Panel A. The total mass — leftovers, asteroids, and comets combined — accreted by the Earth (blue line), Mars (red), and Moon (black). We show two lines for the Moon: the upper one for the 100% retention and the lower one for the 30% retention (Zhu et al., 2019a). The horizontal lines show constraints from the measured HSE abundances assuming that the HSEs were delivered in chondritic proportion: the total accreted masses 3×10^{25} g, 1.6×10^{24} g, and 1.5×10^{22} g for the Earth, Mars, and Moon, respectively. The vertical dot-dashed lines are the Moon-forming impact ($t = 42$ Myr) and estimated time of LMO solidification ($t \sim 200$ Myr). Panel B. The total mass of comets delivered to the Earth. The upper curve shows the profile when spontaneous comet disruptions are ignored. The bottom curve is the cometary flux reduced by a factor of 1.8 to approximately account for disruptions of ~ 100-km-class comets (which presumably bring the bulk of accreted mass). The vertical dot-dashed lines are the instability ($t = 5.8$ Myr) and Moon-forming impact ($t = 42$ Myr) in our model. The horizontal dot-dashed line corresponds to 2×10^{22} g, as required to deliver noble gasses in the Earth atmosphere (Marty et al., 2016). (For interpretation of the references to color in this figure legend, the reader is referred to the web version of this article.)

For example, the initially very massive asteroid belt (Clement et al., 2019); $\sim 1\ M_{\text{Earth}}$), would presumably lead to a much larger (a factor of > 100?) contribution of asteroid impactors to the early impact record. We tested the effects of the radial profile of the planetesimal disk in the terrestrial planet zone and found that the cases with the outer disk edge at $r \sim 1$–1.75 au work quite well to match different constraints (with the mass $\gtrsim 0.1\ M_{\text{Earth}}$ in planetesimals at the time of the gas disk dispersal). Whereas this is broadly consistent with at least some planetesimal formation models (e.g., Izidoro et al., 2021; Morbidelli et al., 2022), the planetesimal population needs to be better characterized (e.g., from the radiometrically calibrated Martian chronology) before a more specific inference can be made.

15. Comparison with previous work

The originality of the present paper consists in explaining the lunar crater record with a physical model that is firmly tied to the terrestrial planet formation and observational constraints. We show that lunar basins were produced by impacts of leftover planetesimals that formed in the terrestrial planet zone — a notable shift from previous theories that invoked E-belt, main-belt asteroids and comets. This has important implications for planet formation: our work constrains the initial mass of planetesimals and identifies planetesimal accretion as the preferred mode of the terrestrial planet growth.

The results address several critical scientific issues, some of which date back to the Apollo program, including the late formation of Imbrium and Orientale, and provide context for the interpretation of classical/empirical impact chronologies. The model impact flux of planetesimals and asteroids on the Earth matches the number of spherule beds found in the late Archean. Cometary impactors provide the right

amount of noble gases for the Earth atmosphere. In a broader context, our work highlights the importance of impacts for the early Earth.

Here we relate our work to two previous publications (Bottke et al., 2007; Brasser et al., 2020) that considered the same general subject — impacts in the early Solar System — but ended up favoring opposing conclusions. We discuss how various assumptions and approximations adopted in these works may have affected the results. Bottke et al. (2007), hereafter B07, studied lunar impacts of leftover planetesimals. They accounted for the collisional evolution of planetesimals and showed how the planetesimal population is reduced by (disruptive) collisions, and that the reduction factor is greater when the initial population is larger. This is the notion of the 'convergent collisional evolution' that we use in this work to calibrate the population of planetesimal impactors from new `Boulder` simulations.

B07 concluded that the leftover planetesimals *cannot* produce basin-scale impacts on the Moon during the Imbrium era, because the collisional and dynamical decline of planetesimal impactors was presumably too quick; by 3.9 Ga, the planetesimal population was reduced by a huge factor in their simulations. Comparing their impact profile with the ones obtained here, we identify the main reason behind this: the planetesimal population in B07 dynamically dropped by two orders of magnitude in 100 Myr and transitioned to a more steady decline after 100 Myr (their Fig. 5). We do not find any such strong initial trend in our work. The problem in question is most likely related to the approximate nature of initial conditions in B07, where the present-day near-Earth asteroids were used as a proxy for terrestrial planetesimals. We note that modern NEAs have relatively short dynamical lifetimes, which may be the main reason behind the fast decline seen in B07 in the first 100 Myr. For comparison, we determine the impact flux from accurate simulations of the terrestrial planet formation (Section 2), and

find that the late lunar impactors were stored on Mars-crossing orbits at 1.2–1.7 au (Section 9).

Brasser et al. (2020), hereafter B20, developed a dynamical model for lunar impactors with four different components: E-belt, asteroid belt, comets and leftover planetesimals.[26] The general methodology used in B20. is similar to that used in the present work (numerical integrations used to construct the impact model). The main methodology-related difference between our work and B20 is that the B20 model is uncalibrated and can (and must, see below, because it does not fit the lunar record) be adjusted to satisfy constraints. Our model is more rigid. All impactor populations in our model were calibrated from independent means (Sections 4 and 5). Our model can either fit or not fit the lunar record — there is no middle ground or room for data-driven adjustment.

Some of the main results in B20 were presented in terms of N_{20} in their Section 5.2 (their Figs. 5 and 8). Here, B20 adjusted their model to match the Neukum's lunar chronology. This was done by assigning weights to leftover planetesimals and E-belt. The best-fit contribution of planetesimals was found to be zero; leftovers were therefore concluded to be only a minor source of lunar impacts. E-belt was assigned a weight equal to ~ 10 (to fit the Neukum chronology). This implies that the E-belt population would have to be increased by a factor of ~ 10 to fit the existing data. B20 proceeded by explaining why this choice may be reasonable.

This can be related to the present work where we found the dominant role of leftover planetesimals — with the standard calibration, no need for any (arbitrary) enhancement. We considered E-belt as an extension of the asteroid belt (this is what the letter E stands for; Bottke et al., 2012) and assumed that it is not justified to arbitrarily increase its initial population if things do not work (Section 4.1). There is no obvious reason for why the initial number density of asteroids immediately below 2 au should have discontinuously increased from that immediately above 2 au. B20 argued that the probability of Rheasilvia basin formation on Vesta would be too low if the E-belt population were not enhanced, but this is simply not the case. In a work dedicated to Vesta's cratering, Roig and Nesvorný (2020) determined a $\sim 50\%$ probability to form Rheasilvia over 4.5 Gyr (with standard assumptions). The Hungaria population, which represents an important constraint on the E-belt (Bottke et al., 2012), was ignored in B20.

B20's asteroid flux is $\sim$10–20 times higher (as explicitly noted in their Section 5.2) than the one obtained here, where we calibrate asteroid impactors on the number of large main belt asteroids observed at the present time (and their orbital distribution; Nesvorný et al., 2017a). This represents an anchor. We use (forward) numerical simulations of asteroids, tie the results to the anchor at the present time, and compute the historical impact flux from that. This is a well-defined calibration method. B20 'calibrated' the E-belt impactors on the lunar crater data, but that presumes that the E-belt was the dominant source of lunar impactors in the first place.

The contribution of asteroids to lunar impacts was simulated in B20 by assuming that all planets formed and remained on their current orbits. This ignored dynamical effects of the outer planet migration/instability. When the outer planet migration/instability is accounted for, the main asteroid belt is depleted by a much larger factor and the impact profile is different (more asteroid impactors early on). B20 therefore underestimated the contribution of the main belt to early lunar impacts (by a factor ~ 100 relative to the enhanced E-belt; compare Fig. 8 in B20 to Fig. 10 in Nesvorný et al. (2017a).

The outer planet migration/instability is needed to reduce the population of inner belt asteroids and match the orbital structure of the asteroid belt (Nesvorný et al., 2017a). It is not explained in B20 how

the lunar impact flux of main belt asteroids was calibrated, and we can only speculate that B20 used the total population that was somewhat similar to that of the present asteroid belt. In any case, the simulation in B20 were not run long enough (only 1 Gyr, not 4.5 Gyr) to demonstrate whether their results were consistent with the present-day asteroid belt.

The lunar N_{20} flux of main-belt asteroids was shown to drop below 10^{-7} by 3.8 Ga in B20 (their Figs. 5 and 8). This indicates that their model would predict $N_{20} < 10^{-7}$ today. For comparison, the present-day lunar N_{20} — as inferred from NEAs and radiometrically dated young lunar surfaces — is estimated $\simeq 10^{-6}$. This shows, even if the E-belt is enhanced by a factor of ~ 10 in B20 to fit the Neukum chronology for $T > 3.5$ Ga, the model is discrepant with the Neukum chronology for $T < 3.5$ Ga (by at least an order of magnitude; the E-belt is not a major source of lunar impacts at the present epoch).

The flux of cometary impactors in B20 drops by roughly three orders of magnitude from 4.5 Ga to 4.3 Ga. This can be contrasted with our results where cometary impacts decline by only a factor of $\simeq 30$ over the same interval. This is most likely caused by the small number statistics in B20. We struggled with this problem ourselves and had to repeatedly increase the resolution of cometary reservoirs to get things right. Eventually, we simulated 100 million comets in Section 4.2 (cloning included). This happens because the impact probability of comets on the Moon is very low ($< 10^{-7}$ per one body starting in the outer disk). When an insufficient resolution is used, very few comets evolve to 1 au late in the simulations and the impact probability computed from the Öpik method is practically zero. B20 results for comets are in direct contradiction to the observed population of present-day Jupiter-family comets, by many orders in magnitude.

The planetesimal population in B20 was taken from simulations published in Brasser et al. (2016). They grouped together planetesimal populations obtained in different formation simulations, replaced the model-generated terrestrial planets with the real ones, and added outer planets. This is not ideal because the solar system is 'not an average of many trial cases' — it is just one realization of the initial conditions. That is why, in our work, we focus on the simulations from Nesvorný et al. (2021a) that best fit various constraints, including planetary masses and orbits, asteroid belt, the Moon-forming impact, etc. The outer planets were included at the start of our simulations (early migration/instability accounted for) and the inner planets did not need to be replaced — practically all their attributes produced in the selected model were accurate.

The collisional evolution of leftover planetesimals was ignored in B20. This is another original component of our work, where the collisional evolution is used to calibrate the population of leftover planetesimals. The planetesimal population is unconstrained if the collisional evolution is not accounted for. In B20, we presume that the planetesimal population was fixed from the HSE constraints (Morbidelli et al., 2018). If so, this would not be consistent with the E-belt dominance in the impact record, as advocated later in their article.

The overall lunar impact flux of planetesimals is underestimated by a factor of ~ 10 in B20 and the impact profile shown for planetesimals in their Fig. 5 is much too steep: it drops by ~ 4 orders of magnitude from 4.5 Ga to 3.8 Ga. This is roughly a factor of 10 faster decline than we obtain in the present work. Again, this is probably related to the insufficient statistics in B20 (we have ~ 4 times better statistics for planetesimals; the need for large statistics was established by convergence studies). If the decline were really that fast, the leftover planetesimals could not produce the Imbrium-era basins, including Imbrium itself. B20 followed planetesimals for only 0.5 Gyr, which did not allow them to address the Imbrium formation. In their Section 4.2.5., B20 suggested that the Imbrium event — for which an E-belt impactor was assumed to be responsible — cannot be ruled at $> 95\%$ confidence. This would imply, if their statement is taken at a face value, that Imbrium was a $\sim 5\%$ probability event in their model — and that is already when the E-belt is enhanced by a factor of ~ 10 in B20 (their nominal model would indicate the $\sim 0.5\%$ probability). For comparison, we estimate

---

[26] Brasser et al. (2021) followed the implications of the model developed in B20 for HSEs. We do not comment on Brasser et al. (2021) here, because B20 is more closely related to our work.

that the Imbrium formation from leftover planetesimals was a ∼ 15–35% probability event, and explain that many more younger/smaller lunar basins than Imbrium would be expected (only two are known: Orientale and Schrödinger), if the probability were much larger than that (Section 9).

B20 did not consider the terrestrial impact flux during the late Archean, and the general impact record in the inner solar system in the last 3.5 Gyr. It is therefore difficult to establish whether their results would satisfy the additional constraints considered in the present work.

16. Summary

We developed an accurate dynamical model that accounts for all major sources of impactors in the inner solar system (leftover planetesimals, asteroids and comets). Each impactor population was calibrated from independent means (not using crater records; Section 3).[27] Here we summarize the main results:

- The leftover planetesimals produced most lunar impacts in the first 1.1 Gyr ($t < 1.1$ Gyr or $T > 3.5$ Ga). Asteroids were the main source of impacts in the last 3.5 Gyr. The transition from leftover planetesimals to asteroids has been imprinted in the crater size distributions (Strom et al., 2005; Head et al., 2010; Orgel et al., 2018). The comet contribution to the crater record is found to be insignificant (for the early instability case adopted here). This would suggest that isotopic and other signatures of comets may be difficult to find on the lunar surface.
- Some 500 $d > 20$ km planetesimals from the terrestrial planet zone (0.5–1.5 au) are expected to impact the Moon since its formation. The early crater record must have been erased plausibly because the lunar surface was unable to support basin-scale impact structures. The ∼ 50 known lunar basins formed after $t \simeq 160$–215 Myr ($T \lesssim 4.36$–4.41 Ga). This is consistent with the long-lived LMO (lunar magma ocean; (Elkins-Tanton et al., 2011; Morbidelli et al., 2018; Zhu et al., 2019a)). The Nectaris basin is estimated to be $T = 4.21$–4.29 Gyr old (from crater counts). The South Pole–Aitken basin should date back to $T = 4.36$–4.41 Ga.
- About two lunar basins are expected to form for $t \gtrsim 650$ Myr ($T \lesssim 3.92$ Ga). The Imbrium basin formation ($T \simeq 3.92$ Ga, $d > 100$ km impactor) is estimated to happen with a ≃ 23% probability in our model. Imbrium should have formed unusually late, relative to the expectations from the lunar impact chronology, to have only two smaller/younger basins than Imbrium (Orientale and Schrödinger); there would be many more younger/smaller basins otherwise (Section 9).
- The Imbrium-era impactors were leftover planetesimals that were stored on orbits with $a \simeq 1.3$-1.7 au, $e < 0.2$, and in the mean motion resonances with Mars (e.g., 6:5, 7:6, 11:9). The resonances provided a phase-protection mechanism against collisions with Mars. The orbits had low eccentricities such that they did not cross the orbit of Earth. The bodies stayed in the resonances for hundreds of Myr and were eventually released to orbits with higher eccentricities. This is an example of the "storage places" hypothesized by Wetherill (1975).
- The lunar and Martian chronologies can be given as a sum of two terms: the stretched exponential function (the leftover planetesimal branch) and a constant (the asteroid or NEA branch). This is similar to the classical (empirical) crater chronologies of Neukum et al. (2001) and Hartmann and Neukum (2001), except that the cratering rate profile in the first ∼ 1 Gyr had a longer tail than the exact exponential. This can lead to modest, ∼ 50 Myr differences in the estimates of lunar basin ages.

- The Martian chronology is found to have a slower decline at late times than the chronologies of the Moon, Earth and Venus. This is a consequence of long dynamical lifetimes of bodies at ∼ 1.5 au — these bodies are more likely to produce late impacts on Mars. Applying the lunar chronology function to Mars can lead to age estimates that can differ, by up to ∼ 500 Myr, from the age estimates obtained from the accurate Martian chronology (Fig. 16A).
- The Noachian/Hesperian and Hesperian/Amazonian boundaries are found to be $T = 3.4$–3.6 Ga and $T = 2.6$–2.9 Ga, respectively (the range given here for $r_{out} = 1$–1.75 au and the standard calibration of leftover planetesimals). The Jezero crater is estimated to be 2.2–2.5 Gyr old for $N_1 = 1.1 \times 10^3$ per 10^6 km^2 or 2.4–2.7 Gyr old for $N_1 = 1.5 \times 10^3$ per 10^6 km^2. The asteroid branch of the Martian chronology ($T \lesssim 2$ Ga) is found to be similar to the chronology developed in Marchi (2021).
- Our model predicts ≃ 20 $d > 10$ km impacts on the Earth for $T = 2.5$–3.5 Ga. This is similar to the number of known spherule beds in the late Archean (Bottke et al., 2012; Johnson et al., 2016a; Marchi et al., 2021). Both the leftover planetesimals and main-belt asteroids contribute to impacts in this time interval. Whereas the asteroid impacts were more uniformly spread over the late Archean, nearly all planetesimal impacts should have happened before 3 Ga.
- The cometary impact profile is more extended in time than thought previously. For example, assuming the instability at $t < 10$ Myr, 90% of impacts happened in the first ≃ 55 Myr, and 99% of impacts happened in the first ≃ 370 Myr. With the Moon-forming impact at $t \sim 50$ Myr ($T \sim 4.52$ Ga), we find that the Earth should have accreted ∼ 1.5–2.5×10^{22} g of cometary material for $T < 4.52$ Ga. This is consistent with comets being the source of noble gasses in the Earth atmosphere (Marty et al., 2016).
- To explain lunar HSEs, we find — in agreement with Morbidelli et al. (2018) and our lunar basin results (Section 8) — that the LMO should have solidified at $t \sim 200$ Myr after the first solar system solids ($T \sim 4.37$ Ga). The mass accreted by the Earth for $t > 50$ Myr is a factor of ∼ 3 too low to explain Earth's HSEs. This shows the need for the stochastic late accretion of very large planetesimals (Bottke et al., 2010).
- Mars would have accreted a factor of ∼ 3 more HSEs for $t > 10$ Myr in our nominal model (the standard calibration of planetesimals and $r_{out} = 1.5$ au) than what is inferred from the SNC meteorites (Marchi et al., 2020). It is possible that: (i) the average abundance of HSEs in the Martian mantle is underestimated (e.g., the SNC meteorites are not representative), (ii) the impactor-retention factor of Mars is smaller than 100%, and/or (iii) the accreted mass was lower because the ring of terrestrial planetesimals was originally confined to 0.5–1 au.

Data availability

Data will be made available on request.

---

[27] Except that we used the crater record to infer at least $\gtrsim 0.1\ M_{Earth}$ in planetesimals in the terrestrial zone at the time of the gas disk dispersal.

References

Andrews-Hanna, J.C., 2016. New Views of the Moon 2, vol. 1911. p. 6061.

Artemieva, N., Ivanov, B., 2004. Icarus 171, 84. http://dx.doi.org/10.1016/j.icarus.2004.05.003.

Barboni, M., Boehnke, P., Keller, C.B., et al., 2017. 48th Annual Lunar and Planetary Science Conference.

Benz, W., Asphaug, E., 1999. Icarus 142, 5. http://dx.doi.org/10.1006/icar.1999.6204.

Bernstein, G.M., Trilling, D.E., Allen, R.L., et al., 2004. Astron. J. 128, 1364. http://dx.doi.org/10.1086/422919.

Bierhaus, E.B., et al., 2018. Secondary craters and ejecta across the solar system: Populations and effects on impact-crater-based chronologies. Meteorit. Planet. Sci. 53, 638–671. http://dx.doi.org/10.1111/maps.13057.

Bottke, W.F., Durda, D.D., Nesvorný, D., et al., 2005. Icarus 175, 111. http://dx.doi.org/10.1016/j.icarus.2004.10.026.

Bottke, W.F., Levison, H.F., Nesvorný, D., et al., 2007. Icarus 190, 203. http://dx.doi.org/10.1016/j.icarus.2007.02.010.

Bottke, W.F., Nolan, M.C., Greenberg, R., et al., 1994. Icarus 107, 255. http://dx.doi.org/10.1006/icar.1994.1021.

Bottke, W.F., Norman, M.D., 2017. Annu. Rev. Earth Planet. Sci. 45, 619. http://dx.doi.org/10.1146/annurev-earth-063016-020131.

Bottke, W.F., Vokrouhlický, D., Ballouz, R.-L., et al., 2020. Astron. J. 160, 14. http://dx.doi.org/10.3847/1538-3881/ab88d3.

Bottke, W.F., Vokrouhlický, D., Minton, D., et al., 2012. Nature 485, 78. http://dx.doi.org/10.1038/nature10967.

Bottke, W.F., Walker, R.J., Day, J.M.D., et al., 2010. Science 330, 1527. http://dx.doi.org/10.1126/science.1196874.

Bouvier, A., Blichert-Toft, J., Moynier, F., et al., 2007. Geochim. Cosmochim. Acta 71, 1583. http://dx.doi.org/10.1016/j.gca.2006.12.005.

Brasser, R., Matsumura, S., Ida, S., et al., 2016. Astrophys. J. 821, 75. http://dx.doi.org/10.3847/0004-637X/821/2/75.

Brasser, R., Mojzsis, S.J., Werner, S.C., et al., 2021. Icarus 361, 114389. http://dx.doi.org/10.1016/j.icarus.2021.114389.

Brasser, R., Werner, S.C., Mojzsis, S.J., 2020. Icarus 338, 113514. http://dx.doi.org/10.1016/j.icarus.2019.113514.

Brož, M., Chrenko, O., Nesvorný, D., et al., 2021. Nat. Astron. 5, 898. http://dx.doi.org/10.1038/s41550-021-01383-3.

Burkhardt, C., Kleine, T., Bourdon, B., et al., 2008. Geochim. Cosmochim. Acta 72, 6177. http://dx.doi.org/10.1016/j.gca.2008.10.023.

Byerly, G.R., Lowe, D.R., Wooden, J.L., Xie, X., 2002. An Archean impact layer from the Pilbara and Kaapvaal cratons. Science 297, 1325–1327. http://dx.doi.org/10.1126/science.1073934.

Canup, R.M., 2012. Science 338, 1052. http://dx.doi.org/10.1126/science.1226073.

Canup, R.M., Righter, K., Dauphas, N., et al., 2021. arXiv:2103.02045.

Chambers, J.E., Wetherill, G.W., 1998. Icarus 136, 304. http://dx.doi.org/10.1006/icar.1998.6007.

Che, X., et al., 2021. Age and composition of young basalts on the Moon measured from samples returned by chang'e-5. Science 374, 887–890. http://dx.doi.org/10.1126/science.abl7957.

Chen, J., Jewitt, D., 1994. Icarus 108, 265. http://dx.doi.org/10.1006/icar.1994.1061.

Clement, M.S., Kaib, N.A., Raymond, S.N., et al., 2018. Icarus 311, 340. http://dx.doi.org/10.1016/j.icarus.2018.04.008.

Clement, M.S., Raymond, S.N., Kaib, N.A., 2019. Astron. J. 157, 38. http://dx.doi.org/10.3847/1538-3881/aaf21e.

Cohen, B.A., Swindle, T.D., Kring, D.A., 2000. Science 290, 1754. http://dx.doi.org/10.1126/science.290.5497.1754.

Collins, G.S., et al., 2020. A steeply-inclined trajectory for the Chicxulub impact. Nature Commun. 11, http://dx.doi.org/10.1038/s41467-020-15269-x.

Culler, T.S., Becker, T.A., Muller, R.A., et al., 2000. Science 287, 1785. http://dx.doi.org/10.1126/science.287.5459.1785.

Dauphas, N., Pourmand, A., 2011. Nature 473, 489. http://dx.doi.org/10.1038/nature10077.

Deienno, R., Izidoro, A., Morbidelli, A., et al., 2018. Astrophys. J. 864, 50. http://dx.doi.org/10.3847/1538-4357/aad55d.

Deienno, R., Walsh, K.J., Kretke, K.A., et al., 2019. Astrophys. J. 876, 103. http://dx.doi.org/10.3847/1538-4357/ab16e1.

DeMeo, F.E., Carry, B., 2013. Icarus 226, 723. http://dx.doi.org/10.1016/j.icarus.2013.06.027.

Di Sisto, R.P., Fernández, J.A., Brunini, A., 2009. Icarus 203, 140. http://dx.doi.org/10.1016/j.icarus.2009.05.002.

Dones, L., Chapman, C.R., McKinnon, W.B., et al., 2009. Saturn from Cassini-Huygens, vol. 613. http://dx.doi.org/10.1007/978-1-4020-9217-6_19.

Elkins-Tanton, L.T., Burgess, S., Yin, Q.-Z., 2011. Earth Planet. Sci. Lett. 304, 326. http://dx.doi.org/10.1016/j.epsl.2011.02.004.

Fassett, C.I., Head, J.W., Kadish, S.J., et al., 2012. J. Geophys. Res. Planets 117, E00H06. http://dx.doi.org/10.1029/2011JE003951.

Fraser, W.C., Brown, M.E., Morbidelli, A., et al., 2014. Astrophys. J. 782, 100. http://dx.doi.org/10.1088/0004-637X/782/2/100.

Glass, B.P., Simonson, B.M., 2013. Distal Impact Ejecta Layers: A Record of Large Impacts in Sedimentary Deposits. Springer.

Gomes, R., Levison, H.F., Tsiganis, K., et al., 2005. Nature 435, 466. http://dx.doi.org/10.1038/nature03676.

Gomes, R.S., Morbidelli, A., Levison, H.F., 2004. Icarus 170, 492. http://dx.doi.org/10.1016/j.icarus.2004.03.011.

Grange, M.L., Pidgeon, R.T., Nemchin, A.A., Timms, N.E., Meyer, C., 2013. Interpreting U-Pb data from primary and secondary features in lunar zircon. Geochim. Cosmochim. Acta 101, 112–132. http://dx.doi.org/10.1016/j.gca.2012.10.013.

Granvik, M., Morbidelli, A., Jedicke, R., et al., 2018. Icarus 312, 181. http://dx.doi.org/10.1016/j.icarus.2018.04.018.

Hansen, B.M.S., 2009. Formation of the terrestrial planets from a narrow annulus. Astrophys. J. 703, 1131–1140. http://dx.doi.org/10.1088/0004-637X/703/1/1131.

Harris, A.W., D'Abramo, G., 2015. Icarus 257, 302. http://dx.doi.org/10.1016/j.icarus.2015.05.004.

Hartmann, W.K., 1966. Icarus 5, 406. http://dx.doi.org/10.1016/0019-1035(66)90054-6.

Hartmann, W.K., 2005. Martian cratering 8: Isochron refinement and the chronology of Mars. Icarus 174, 294–320. http://dx.doi.org/10.1016/j.icarus.2004.11.023.

Hartmann, W.K., 2019. Geosciences 9, 285. http://dx.doi.org/10.3390/geosciences9070285.

Hartmann, W.K., Neukum, G., 2001. Space Sci. Rev. 96, 165. http://dx.doi.org/10.1023/A:1011945222010.

Hartmann, W.K., Quantin, C., Mangold, N., 2007. Icarus 186, 11. http://dx.doi.org/10.1016/j.icarus.2006.09.009.

Hartung, J.B., 1974. Meteoritics 9, 349.

Head, J.W., Fassett, C.I., Kadish, S.J., et al., 2010. Science 329, 1504. http://dx.doi.org/10.1126/science.1195050.

Hiesinger, H., van der Bogert, C.H., Iqbal, W., Gebbing, T., 2020. The lunar chronology: A status report. In: 51st Annual Lunar and Planetary Science Conference.

Hiesinger, H., van der Bogert, C.H., Pasckert, J.H., Plescia, J.B., Robinson, M.S., 2016. Impact chronology of the Moon — results from the lunar reconnaissance orbiter camera (LROC). In: New Views of the Moon, vol. 2.

Hiesinger, H., et al., 2012. How old are young lunar craters? J. Geophys. Res. Planets 117, http://dx.doi.org/10.1029/2011JE003935.

Holsapple, K.A., Housen, K.R., 2007. Icarus 187, 345. http://dx.doi.org/10.1016/j.icarus.2006.08.029.

Huang, Y.-H., Minton, D.A., Zellner, N.E.B., Hirabayashi, M., Richardson, J.E., Fassett, C.I., 2018. No change in the recent lunar impact flux required based on modeling of impact glass spherule age distributions. Geophys. Res. Lett. 45, 6805–6813. http://dx.doi.org/10.1029/2018GL077254.

Izidoro, A., Dasgupta, R., Raymond, S.N., et al., 2021. Nature Astron. http://dx.doi.org/10.1038/s41550-021-01557-z.

Jacobson, S.A., Morbidelli, A., 2014. Philos. Trans. R. Soc. Lond. Ser. A 372, 0174. http://dx.doi.org/10.1098/rsta.2013.0174.

Jacobson, S.A., Rubie, D.C., Hernlund, J., et al., 2017. Earth Planet. Sci. Lett. 474, 375. http://dx.doi.org/10.1016/j.epsl.2017.06.023.

Johansen, A., Ronnet, T., Bizzarro, M., et al., 2021. Sci. Adv. 7, eabc0444. http://dx.doi.org/10.1126/sciadv.abc0444.

Johnson, B.C., Blair, D.M., Collins, G.S., et al., 2016b. Science 354, 441. http://dx.doi.org/10.1126/science.aag0518.

Johnson, B.C., Collins, G.S., Minton, D.A., et al., 2016a. Icarus 271, 350. http://dx.doi.org/10.1016/j.icarus.2016.02.023.

Johnson, B.C., Melosh, H.J., 2012. Impact spherules as a record of an ancient heavy bombardment of Earth. Nature 485, 75–77. http://dx.doi.org/10.1038/nature10982.

Kenyon, S.J., Bromley, B.C., 2001. Astron. J. 121, 538. http://dx.doi.org/10.1086/318019.

Kirchoff, M.R., Marchi, S., Bottke, W.F., et al., 2021. Icarus 355, 114110. http://dx.doi.org/10.1016/j.icarus.2020.114110.

Kleine, T., Walker, R.J., 2017. Annu. Rev. Earth Planet. Sci. 45, 389. http://dx.doi.org/10.1146/annurev-earth-063016-020037.

Kring, D.A., Cohen, B.A., 2002. J. Geophys. Res. Planets 107, 5009. http://dx.doi.org/10.1029/2001JE001529.

Kruijer, T.S., Archer, G.J., Kleine, T., 2021. No ^{182}W evidence for early Moon formation. Nat. Geosci. 14, 714–715. http://dx.doi.org/10.1038/s41561-021-00820-2.

Le Feuvre, M., Wieczorek, M.A., 2011. Icarus 214, 1. http://dx.doi.org/10.1016/j.icarus.2011.03.010.

Leinhardt, Z.M., Stewart, S.T., 2012. Astrophys. J. 745, 79. http://dx.doi.org/10.1088/0004-637X/745/1/79.

Levison, H.F., Dones, L., Chapman, C.R., et al., 2001. Icarus 151, 286. http://dx.doi.org/10.1006/icar.2001.6608.

Levison, H.F., Duncan, M.J., 1994. Icarus 108, 18. http://dx.doi.org/10.1006/icar.1994.1039.

Levison, H.F., Duncan, M.J., 1997. Icarus 127, 13. http://dx.doi.org/10.1006/icar.1996.5637.

Levison, H.F., Morbidelli, A., Dones, L., et al., 2002. Science 296, 2212. http://dx.doi.org/10.1126/science.1070226.

Li, Q.-L., Zhou, Q., Liu, Y., et al., 2021. Nature 600, 54. http://dx.doi.org/10.1038/s41586-021-04100-2.

Liu, B., Raymond, S.N., Jacobson, S.A., 2022. Nature 604, 643. http://dx.doi.org/10.1038/s41586-022-04535-1.

Lowe, D.R., Byerly, G.R., 1986. Early Archean silicate spherules of probable impact origin, South Africa and Western Australia. Geology 14, 83.

Lowe, D.R., Byerly, G.R., Kyte, F.T., 2014. Recently discovered 3.42-3.23 Ga impact layers, Barberton Belt, South Africa: 3.8 Ga detrital zircons, Archean impact history, and tectonic implications. Geology 42, 747–750. http://dx.doi.org/10.1130/G35743.1.

Mainzer, A.K., Bauer, J.M., Cutri, R.M., et al., 2019. NASA Planet. Data Syst. http://dx.doi.org/10.26033/18S3-2Z54.

Marchi, S., 2021. Astron. J. 161, 187. http://dx.doi.org/10.3847/1538-3881/abe417.

Marchi, S., Bottke, W.F., Elkins-Tanton, L.T., et al., 2014. Nature 511, 578. http://dx.doi.org/10.1038/nature13539.

Marchi, S., Bottke, W.F., Kring, D.A., et al., 2012. Earth Planet. Sci. Lett. 325, 27. http://dx.doi.org/10.1016/j.epsl.2012.01.021.

Marchi, S., Drabon, N., Schulz, T., et al., 2021. Nat. Geosci. 14, 827. http://dx.doi.org/10.1038/s41561-021-00835-9.

Marchi, S., Mottola, S., Cremonese, G., et al., 2009. Astron. J. 137, 4936. http://dx.doi.org/10.1088/0004-6256/137/6/4936.

Marchi, S., Walker, R.J., Canup, R.M., 2020. Sci. Adv. 6, eaay2338. http://dx.doi.org/10.1126/sciadv.aay2338.

Marty, B., Avice, G., Sano, Y., et al., 2016. Earth Planet. Sci. Lett. 441, 91. http://dx.doi.org/10.1016/j.epsl.2016.02.031.

Maurice, M., Tosi, N., Schwinger, S., et al., 2020. Sci. Adv. 6, eaba8949. http://dx.doi.org/10.1126/sciadv.aba8949.

Mazrouei, S., Ghent, R.R., Bottke, W.F., et al., 2019. Science 363, 253. http://dx.doi.org/10.1126/science.aar4058.

Merle, R.E., Nemchin, A.A., Grange, M.L., et al., 2013. 44th Annual Lunar and Planetary Science Conference.

Meyer, J., Elkins-Tanton, L., Wisdom, J., 2010. Icarus 208, 1. http://dx.doi.org/10.1016/j.icarus.2010.01.029.

Miljković, K., Collins, G.S., Wieczorek, M.A., et al., 2016. J. Geophys. Res. Planets 121, 1695. http://dx.doi.org/10.1002/2016JE005038.

Miljković, K., Wieczorek, M.A., Collins, G.S., et al., 2013. Science 342, 724. http://dx.doi.org/10.1126/science.1243224.

Miljković, K., Wieczorek, M.A., Laneuville, M., et al., 2021. Nature Commun. 12, 5433. http://dx.doi.org/10.1038/s41467-021-25818-7.

Minton, D.A., Richardson, J.E., Fassett, C.I., 2015. Icarus 247, 172. http://dx.doi.org/10.1016/j.icarus.2014.10.018.

Morbidelli, A., Baillié, K., Batygin, K., et al., 2022. Nat. Astron. 6, 72. http://dx.doi.org/10.1038/s41550-021-01517-7.

Morbidelli, A., Bottke, W.F., Nesvorný, D., et al., 2009a. Icarus 204, 558. http://dx.doi.org/10.1016/j.icarus.2009.07.011.

Morbidelli, A., Delbo, M., Granvik, M., et al., 2020. Icarus 340, 113631. http://dx.doi.org/10.1016/j.icarus.2020.113631.

Morbidelli, A., Levison, H.F., Bottke, W.F., et al., 2009b. Icarus 202, 310. http://dx.doi.org/10.1016/j.icarus.2009.02.033.

Morbidelli, A., Nesvorny, D., Laurenz, V., et al., 2018. Icarus 305, 262. http://dx.doi.org/10.1016/j.icarus.2017.12.046.

Nakajima, M., Stevenson, D.J., 2014. Icarus 233, 259. http://dx.doi.org/10.1016/j.icarus.2014.01.008.

Nesvorný, D., 2018. Annu. Rev. Astron. Astrophys. 56, 137. http://dx.doi.org/10.1146/annurev-astro-081817-052028.

Nesvorný, D., Bottke, W.F., Marchi, S., 2021a. Icarus 368, 114621. http://dx.doi.org/10.1016/j.icarus.2021.114621.

Nesvorný, D., Deienno, R., Bottke, W.F., et al., NEOMOD: a new orbital distribution model for near earth asteroids, Icarus.

Nesvorný, D., Roig, F., Bottke, W.F., 2017a. Astron. J. 153, 103. http://dx.doi.org/10.3847/1538-3881/153/3/103.

Nesvorný, D., Roig, F.V., Deienno, R., 2021b. Astron. J. 161, 50. http://dx.doi.org/10.3847/1538-3881/abc8ef.

Nesvorný, D., Roig, F.V., Vokrouhlický, D., et al., 2022. Astrophys. J. Lett. 941, L9. http://dx.doi.org/10.3847/2041-8213/aca40e.

Nesvorný, D., Vokrouhlický, D., 2019. Icarus 331, 49. http://dx.doi.org/10.1016/j.icarus.2019.04.030.

Nesvorný, D., Vokrouhlický, D., Alexandersen, M., et al., 2020. Astron. J. 160, 46. http://dx.doi.org/10.3847/1538-3881/ab98fb.

Nesvorný, D., Vokrouhlický, D., Dones, L., et al., 2017b. Astrophys. J. 845, 27. http://dx.doi.org/10.3847/1538-4357/aa7cf6.

Nesvorný, D., Vokrouhlický, D., Stern, A.S., et al., 2019. Astron. J. 158, 132. http://dx.doi.org/10.3847/1538-3881/ab3651.

Neukum, G., Ivanov, B.A., 1994. Hazards Due to Comets and Asteroids. p. 359.

Neukum, G., Ivanov, B.A., Hartmann, W.K., 2001. Space Sci. Rev. 96, 55. http://dx.doi.org/10.1023/A:1011989004263.

Neumann, G.A., Zuber, M.T., Wieczorek, M.A., et al., 2015. Sci. Adv. 1, e1500852. http://dx.doi.org/10.1126/sciadv.1500852.

Orgel, C., Michael, G., Fassett, C.I., et al., 2018. J. Geophys. Res. Planets 123, 748. http://dx.doi.org/10.1002/2017JE005451.

Ozdemir, S., Schulz, T., Acken, D.van., Luguet, A., Reimold, W.U., Koeberl, C., 2019. Meteoritic highly siderophile element and re-os isotope signatures of archean spherule layers from the CT3 drill core, barberton greenstone belt, South Africa. Meteorit. Planet. Sci. 54, 2203–2216. http://dx.doi.org/10.1111/maps.13234.

Pidgeon, R.T., Nemchin, A.A., Grange, M.L., Meyer, C., 2010. Evidence for a Lunar "Cataclysm" at 4.34 Ga from Zircon U-Pb Systems. 41st Annual Lunar and Planetary Science Conference.

Popova, O., Nemtchinov, I., Hartmann, W.K., 2003. MAPS 38, 905. http://dx.doi.org/10.1111/j1945-5100.2003.tb00287.x.

Raymond, S.N., Nesvorny, D., 2020. arXiv:2012.07932.

Robbins, S.J., 2014. Earth Planet. Sci. Lett. 403, 188. http://dx.doi.org/10.1016/j.epsl.2014.06.038.

Robbins, S.J., 2022. Planet. Sci. J. 3, 274. http://dx.doi.org/10.3847/PSJ/aca282.

Roig, F., Nesvorný, D., 2015. Astron. J. 150, 186. http://dx.doi.org/10.1088/0004-6256/150/6/186.

Roig, F., Nesvorný, D., 2020. Astron. J. 160, 110. http://dx.doi.org/10.3847/1538-3881/aba750.

Rubie, D.C., Laurenz, V., Jacobson, S.A., et al., 2016. Science 353, 1141. http://dx.doi.org/10.1126/science.aaf6919.

Ryder, G., 1990. EOS Trans. 71, 313. http://dx.doi.org/10.1029/90EO00086.

Ryder, G., 2002. J. Geophys. Res. Planets 107, 5022. http://dx.doi.org/10.1029/2001JE001583.

Schultz, P.H., Crawford, D.A., 2016. Nature 535, 391. http://dx.doi.org/10.1038/nature18278.

Schulz, T., et al., 2017. New constraints on the Paleoarchean meteorite bombardment of the Earth—Geochemistry and Re–Os isotope signatures of the BARB5 ICDP drill core from the Barberton Greenstone Belt, South Africa. Geochim. Cosmochim. Acta 211, 322–340.

Shahrzad, S., Kinch, K.M., Goudge, T.A., et al., 2019. Geophys. Res. Lett. 46, 2408. http://dx.doi.org/10.1029/2018GL081402.

Shearer, C.K., 2006. Remnants of a Magma Ocean. Insights into the Early Differentiation of the Moon and Its Relevance to the Differentiation of the Terrestrial Planets. Workshop on Early Planetary Differentiation 1335, 94–95.

Spudis, P.D., 1993. The geology of multi-ring impact basins. In: Camb. Planet. Sci. Ser., vol. 8, Cambridge University Press, ISBN: 0521261031.

Stöffler, D., Ryder, G., 2001. Space Sci. Rev. 96, 9. http://dx.doi.org/10.1023/A:1011937020193.

Strom, R.G., Malhotra, R., Ito, T., et al., 2005. Science 309, 1847. http://dx.doi.org/10.1126/science.1113544.

Tanaka, K.L., 1986. J. Geophys. Res. 91, E139. http://dx.doi.org/10.1029/JB091iB13p0E139.

Tera, F., Papanastassiou, D.A., Wasserburg, G.J., 1974. Earth Planet. Sci. Lett. 22, 1. http://dx.doi.org/10.1016/0012-821X(74)90059-4.

Thiemens, M.M., Sprung, P., Fonseca, R.O.C., et al., 2019. Nat. Geosci. 12, 696. http://dx.doi.org/10.1038/s41561-019-0398-3.

Thiemens, M.M., et al., 2021. Reply to: No ^{182}W evidence for early Moon formation. Nat. Geosci. 14, 716–718. http://dx.doi.org/10.1038/s41561-021-00821-1.

Tsiganis, K., Gomes, R., Morbidelli, A., Levison, H.F., 2005. Origin of the orbital architecture of the giant planets of the solar system. Nature 435, 459–461. http://dx.doi.org/10.1038/nature03539.

Vokrouhlický, D., Bottke, W.F., Chesley, S.R., et al., 2015. Asteroids IV, vol. 509. http://dx.doi.org/10.2458/azu_uapress_9780816532131-ch02.

Vokrouhlický, D., Nesvorný, D., Dones, L., 2019. Astron. J. 157, 181. http://dx.doi.org/10.3847/1538-3881/ab13aa.

Warner, N.H., Schuyler, A.J., Rogers, A.D., et al., 2020. Geophys. Res. Lett. 47, e89607. http://dx.doi.org/10.1029/2020GL089607.

Weidenschilling, S.J., Spaute, D., Davis, D.R., et al., 1997. Icarus 128, 429. http://dx.doi.org/10.1006/icar.1997.5747.

Werner, S.C., Ody, A., Poulet, F., 2014. Science 343, 1343. http://dx.doi.org/10.1126/science.1247282.

Wetherill, G.W., 1975. Lunar and Planetary Science Conference Proceedings, vol. 2, pp. 1539.

Wetherill, G.W., 1990. Annu. Rev. Earth Planet. Sci. 18, 205. http://dx.doi.org/10.1146/annurev.ea.18.050190.001225.

Wilhelms, D.E., McCauley, J.F., Trask, N.J., 1987. For sale by the Books and Open-file Reports Section, U.S. Geological Survey. Washington U.S. G.P.O.; Denver, CO (Federal Center, Box 25425, Denver 80225).

Williams, J.P., Cieza, L.A., 2011. Annu. Rev. Astron. Astrophys. 49, 67. http://dx.doi.org/10.1146/annurev-astro-081710-102548.

Wisdom, J., Holman, M., 1991. Astron. J. 102, 1528. http://dx.doi.org/10.1086/115978.

Wishard, C., Minton, D., Singh, J., 2022. Size-dependent decay of accretion populations. In: AAS/Division for Planetary Sciences Meeting Abstracts.

Youdin, A.N., Goodman, J., 2005. Astrophys. J. 620, 459. http://dx.doi.org/10.1086/426895.

Zahnle, K., Schenk, P., Levison, H., et al., 2003. Icarus 163, 263. http://dx.doi.org/10.1016/S0019-1035(03)00048-4.

Zellner, N.E.B., Delano, J.W., 2015. ^{40}Ar/^{39}Ar ages of lunar impact glasses: Relationships among Ar diffusivity, chemical composition, shape, and size. Geochim. Cosmochim. Acta 161, 203–218. http://dx.doi.org/10.1016/j.gca.2015.04.013.

Zhang, B., Lin, Y., Moser, D.E., et al., 2019. J. Geophys. Res. Planets 124, 3205. http://dx.doi.org/10.1029/2019JE005992.

Zhu, M.-H., Artemieva, N., Morbidelli, A., et al., 2019a. Nature 571, 226. http://dx.doi.org/10.1038/s41586-019-1359-0.

Zhu, M.-H., Wünnemann, K., Potter, R.W.K., et al., 2019b. J. Geophys. Res. Planets 124, 2117. http://dx.doi.org/10.1029/2018JE005826.